

A Linear Strain, Curvature-Driven Triangular Element for the Analysis of Membrane Structures

P.D.Gosling¹ and L. Zhang¹

Abstract: The analysis of membrane structures is made complex by the essentially anti-clastic geometry and flexibility introducing significant geometric nonlinearities. With the increasing application of these structures in high-profile projects, the introduction of new materials in the form of ETFE foil, for example, and the impending requirements of a membrane structures-specific Eurocode, the need for high quality analysis capabilities is paramount. Existing formulations lag behind shell element counterparts and are based on a range of principles, from discrete to continua, and uniaxial to plane stress constitutive laws. In this paper, we present a linear strain triangular element for the efficient and accurate analysis of membrane structures. The triangular geometry of the element meets typical patterning needs, whilst the novel inclusion of curvature means that each element closely matches the characteristics of the local surface of the membrane efficiently. This is achieved without the introduction of rotational degrees-of-freedom, therefore negating bending stiffnesses that may compromise the quality of the simulation. The element is also shown to work well in predicting the onset and development of wrinkling.

Keywords: Membrane structure analysis; linear strain formulation; dynamic relaxation.

1 Introduction - membrane structure analysis and design: principles and practice

Modern fabric structures(fig.1) designed for permanent purposes have been developed with increasing popularity since the 1950s. Compared with ancient fabric forms, higher requirements in both aesthetics and structural stability must be satisfied in modern fabric structures. The key mechanism to achieve the increased performance is correct generation of tensile forces to induce smooth geometries to

¹Newcastle University, School of Civil Engineering & Geosciences, Drummond Building, Newcastle-upon-Tyne, NE1 7RU, UK

create what are now termed "tensile structures".



Figure 1: Price Waterhouse - Cooper building, Brussels,2003

Fabric materials have little compression or bending stiffness. They are, therefore, prone to fold and wrinkle under external forces when not adequately tensioned by pretension. The applied pretension stresses can largely improve the stability and stiffness of the fabric surface, and the negative strain produced by loads can be compensated by the initial positive strain due to pretensions. However, the prestress required to ensure the structural performance of the canopy may not be realised in the physical structure for a number of reasons, including accuracy of the numerical analysis system. Wrinkles are an obvious physical indicator that the required stress state is not present, and effectively state that the canopy is not working as intended.

The analysis of membrane-type structures was not a priority during the initial development of the finite element method. Challenges in the field of numerical simulation were more associated with plates and shells, material non-linearity, and dynamics. Geometric non-linearity was also not a major focus of research in a de-

velopment context as it was less significant than plasticity for many engineering applications. This is with the exception of aeronautical engineering, for example, but where geometric non-linearity is associated with plates and shells as opposed to purely membrane-type structural responses.

A number of numerical approaches have been developed for the analysis of membrane. These range from the representation of the continuum in the form of a discretisation of cable or bar-type elements (e.g. Schek, H.J., (1973), Barnes, M.R., (1980)), through to more sophisticated plane-stress formulations (e.g. Gosling, P.D. et al, (1996), Valdes, J.G., et al, (2009)). The solutions to the non-linear equations arising from these formulations are obtained from the force-density approach (e.g. Pauletti, R.M.O. (2008)), dynamic relaxation (e.g. Day, A.S., (1965), Kashiwa, M., (2009)), or classical finite element techniques (e.g. Miller et al, (1985), Bletzinger, K.-U. et al, (2008)).

The performance of a membrane structure is well known to be directly related to the magnitudes of the principal curvatures (Bridgens, B.N., et al, (2004), Forster, B.F., et al, (2004)). In many numerical simulation approaches, the membrane surface is discretised into facets using either a mesh of constant strain triangles (CST, e.g. Barnes M.R., (1999)) or approximately orthogonal cables and bars (e.g. Grundig, L., (1988)), and where the degrees-of-freedom are purely translational. For such numerical models the curvatures are only implicit in the finite element formulation, in that they may be calculated at the termination of the analysis, and do not contribute to the solution procedure.

A six-node linear strain triangle element with curvatures is introduced by Ye Xiaobing (Ye Xiaobing, (1998)). In his formulation, the curvatures terms used in thin shell theory is applied into the fabric structure analysis. He pointed out that in the existing standard 2-D element, the element stiffness perpendicular to the element plane is only contributed from the high order part of the Green Strain, which is small and may cause the serious inefficiency of the geometry-nonlinear structural analysis with large deformations (e.g form-finding). As Eqn.1, he modified the Green Strain formula with additional strain resulted by the products of curvatures and deflections, therefore the element stiffness is significantly enhanced to the load vector perpendicular to the element plane. The curvatures are calculated based on the geometry and deformation, then there is no significantly extra computing cost for the inclusion of the curvatures.

$$\begin{aligned}\varepsilon_X &= \frac{\partial U}{\partial X} + K_{\bar{X}}W + \frac{1}{2} \left[\left(\frac{\partial U}{\partial X} \right)^2 + \left(\frac{\partial V}{\partial X} \right)^2 + \left(\frac{\partial W}{\partial X} \right)^2 \right] \\ \varepsilon_Y &= \frac{\partial V}{\partial Y} + K_{\bar{Y}}W + \frac{1}{2} \left[\left(\frac{\partial U}{\partial Y} \right)^2 + \left(\frac{\partial V}{\partial Y} \right)^2 + \left(\frac{\partial W}{\partial Y} \right)^2 \right]\end{aligned}$$

$$\begin{aligned}\gamma_{XY} &= \\ \frac{\partial U}{\partial Y} + \frac{\partial V}{\partial X} + 2K_{\bar{XY}}W &+ \left(\frac{\partial U}{\partial X} \right) \left(\frac{\partial U}{\partial Y} \right) + \left(\frac{\partial V}{\partial X} \right) \left(\frac{\partial V}{\partial Y} \right) + \left(\frac{\partial W}{\partial X} \right) \left(\frac{\partial W}{\partial Y} \right)\end{aligned}\tag{1}$$

However the modified formula does not give the same strain values as the standard Green Strain for a curved element geometry with large deflections. The numerical comparison(Ye Xiaobing, (1998)) shows that the linear strain element model does not yield the same results by the constant strain triangle model using the standard Green Strain definition. In this paper we extend the concept proposed by Ye Xiaobing (Ye Xiaobing, (1998)) by maintaining original Green strain formula while linking the element stresses and nodal force perpendicular to the element surface by the curvatures. Therefore the linear strain triangle element with the enhanced stiffness yields the same results as the ones by other types of standard 2-D element, that is demonstrated in the section 9.

The conception of the element curvature is introduced in section.2, and the mathematical details are given in section. The performance of the element is demonstrated through the analysis of a number of benchmark-type problems. The performance of the element is demonstrated through the analysis of a number of benchmark-type problems. The capabilities of the element are also shown to be extended to wrinkling for which the onset and development of wrinkles are predicted.

2 The conception of the fabric element curvature

The need of the curvatures terms for the linear strain triangle element can be demonstrated using the following example. As show in the figure 2, a cylinder fabric membrane with a radius of R is under a uniform air pressure load p on its inner face, which is balanced by the membrane stress f along the hoop direction. The

mechanical relationship between p and f can be easily estimated analytically. The membrane surface can be modelled using constant strain and linear strain triangles separately. Assuming that the nodal forces generated from the element stresses are along the element surface, as illustrated in figure 2, the air pressure is balanced by the force vectors combined from the nodal forces of two adjacent CST element. In contrast, in the linear strain element model, the nodal forces generated by the element stresses may be eliminated by the joining element if the mesh is symmetric, therefore the force balance is unlikely to be achieved at the joint nodes.

In that situation, the existing standard 2-D triangle element does not provide a direct link between surface stresses and the perpendicular nodal force. The new relation-

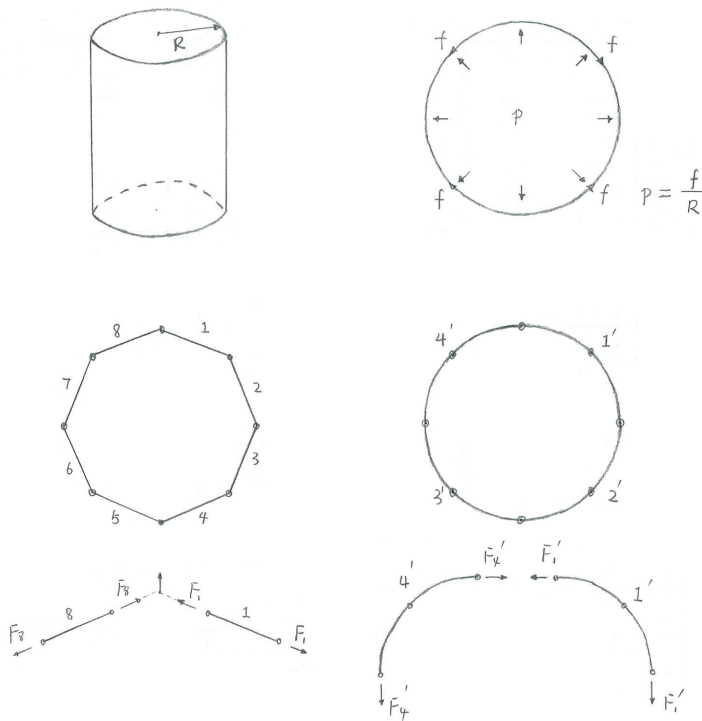


Figure 2: A membrane cylinder modeled by constant strain and linear strain triangle

ship between the element stresses and nodal forces is necessary to be created to enable the linear strain element to smoothly simulate a curved fabric surface. In this paper, biaxial curvatures and torsions calculated based on the element geometry are included in the element formulation without adding degree of freedom. The formulation details is given in section. 3.

3 Fundamental geometrical properties & definitions

3.1 Local co-ordinate system

A curved plane element (fig.3) is defined by a the local tangent co-ordinate system, XY , where it is assumed that the X direction is aligned with the principal membrane material direction (e.g. warp). The Z axis is established normal to the XY plane. For any point on the surface, the co-ordinate vector may be expressed in the global system as $\bar{R} = \bar{R}(x, y, z)$.

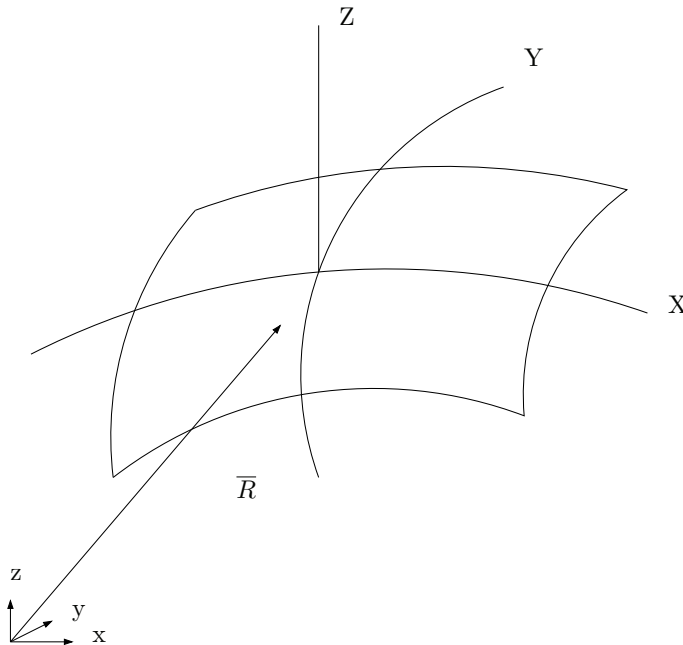


Figure 3: Local Curved Co-ordinate System

To facilitate transformation of the local to the global system, a second local co-ordinate system $\bar{X}, \bar{Y}, \bar{Z}$ is introduced, in which the plane \bar{X}, \bar{Y} is defined by the position of the apex nodes 1, 2, 3 as shown in figure 4.

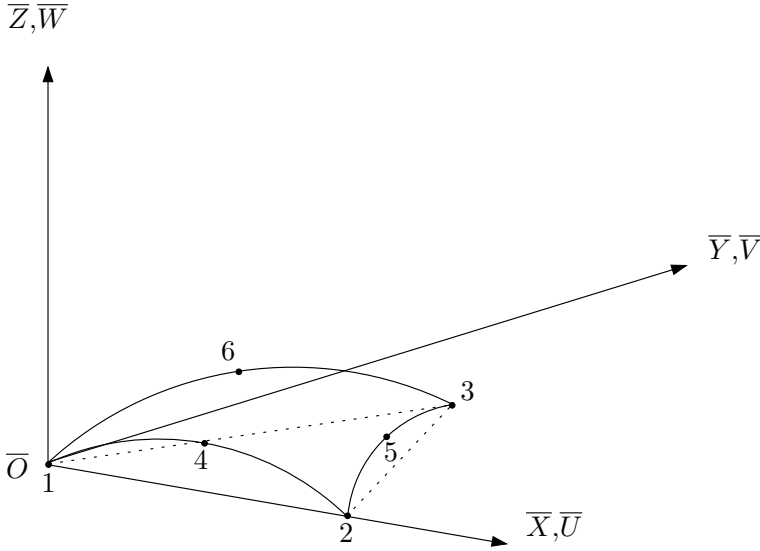


Figure 4: Curvilinear co-ordinate system

The transformation matrix between these two local co-ordinate systems is expressed as,

$$\begin{Bmatrix} F_{\bar{X}} \\ F_{\bar{Y}} \\ F_{\bar{Z}} \end{Bmatrix} = \bar{T}^c \begin{Bmatrix} F_X \\ F_Y \\ F_Z \end{Bmatrix}, \begin{Bmatrix} \bar{U} \\ \bar{V} \\ \bar{W} \end{Bmatrix} = \bar{T}^c \begin{Bmatrix} U \\ V \\ W \end{Bmatrix} \quad (2)$$

where,

$$\bar{T}^c = \begin{bmatrix} \frac{1}{\sqrt{1+(\bar{Z},\bar{X})^2}} & 0 & \frac{-\bar{Z},\bar{X}}{\sqrt{1+(\bar{Z},\bar{X})^2}} \\ 0 & \frac{1}{\sqrt{1+(\bar{Z},\bar{Y})^2}} & \frac{-\bar{Z},\bar{Y}}{\sqrt{1+(\bar{Z},\bar{Y})^2}} \\ \frac{\bar{Z},\bar{X}\sqrt{(1+(\bar{Z},\bar{X})^2)(1+(\bar{Z},\bar{Y})^2)}}{\sqrt{1+(\bar{Z},\bar{X})^2+(\bar{Z},\bar{Y})^2}} & \frac{\bar{Z},\bar{Y}\sqrt{(1+(\bar{Z},\bar{X})^2)(1+(\bar{Z},\bar{Y})^2)}}{\sqrt{1+(\bar{Z},\bar{X})^2+(\bar{Z},\bar{Y})^2}} & \frac{\sqrt{(1+(\bar{Z},\bar{X})^2)(1+(\bar{Z},\bar{Y})^2)}}{\sqrt{1+(\bar{Z},\bar{X})^2+(\bar{Z},\bar{Y})^2}} \end{bmatrix} \quad (3)$$

in which \bar{Z},\bar{X} and \bar{Z},\bar{Y} are the derivatives of \bar{Z} with respect to \bar{X} and \bar{Y} respectively. Consistent with the number of nodes describing the element, we assume the curved surface can be represented by the complete polynomial,

$$\bar{Z} = a_1 + a_2\bar{X} + a_3\bar{Y} + a_4\bar{X}^2 + a_5\bar{X}\bar{Y} + a_6\bar{Y}^2 \quad (4)$$

Substituting the co-ordinates of the 6 element nodes into Eqn. 4, we obtain,

$$\begin{bmatrix} 1 & \bar{X}_1 & \bar{Y}_1 & \bar{X}_1^2 & \bar{X}_1\bar{Y}_1 & \bar{Y}_1^2 \\ 1 & \bar{X}_2 & \bar{Y}_2 & \bar{X}_2^2 & \bar{X}_2\bar{Y}_2 & \bar{Y}_2^2 \\ 1 & \bar{X}_3 & \bar{Y}_3 & \bar{X}_3^2 & \bar{X}_3\bar{Y}_3 & \bar{Y}_3^2 \\ 1 & \bar{X}_4 & \bar{Y}_4 & \bar{X}_4^2 & \bar{X}_4\bar{Y}_4 & \bar{Y}_4^2 \\ 1 & \bar{X}_5 & \bar{Y}_5 & \bar{X}_5^2 & \bar{X}_5\bar{Y}_5 & \bar{Y}_5^2 \\ 1 & \bar{X}_6 & \bar{Y}_6 & \bar{X}_6^2 & \bar{X}_6\bar{Y}_6 & \bar{Y}_6^2 \end{bmatrix} \cdot \begin{Bmatrix} a_1 \\ a_2 \\ a_3 \\ a_4 \\ a_5 \\ a_6 \end{Bmatrix} = \begin{Bmatrix} \bar{Z}_1 \\ \bar{Z}_2 \\ \bar{Z}_3 \\ \bar{Z}_4 \\ \bar{Z}_5 \\ \bar{Z}_6 \end{Bmatrix} \quad (5)$$

or

$$[\bar{A}] \cdot \{a\} = \{\bar{Z}\}$$

Solving Eqn. 5, then

$$\{a\} = [\bar{A}]^{-1} \{\bar{Z}\} \quad (6)$$

where the values of a_1 – a_6 are calculated numerically for each element.

As the surface of the element is curved, the co-ordinates of any point on the surface of the element are defined by arc lines over the element surface. Therefore, the curvilinear co-ordinates (X, Y) are defined with a local origin at the geometric centre of the element as,

$$\begin{aligned} X &= \int_0^{\bar{X}} \sqrt{1 + \left(\frac{\partial \bar{Z}}{\partial \bar{X}}\right)^2} d\bar{X} \\ &= \int_0^{\bar{X}} \sqrt{1 + (a_2 + 2a_4\bar{X} + a_5\bar{Y})^2} d\bar{X} \\ &= \left(\frac{a_2 + a_5\bar{Y}}{4a_4} + \frac{\bar{X}}{2}\right) \cdot \sqrt{1 + (a_2 + 2a_4\bar{X} + a_5\bar{Y})^2} + \frac{\operatorname{arcsinh}(a_2 + 2a_4\bar{X} + a_5\bar{Y})}{4a_4} \quad (7) \end{aligned}$$

$$Y = \int_0^{\bar{Y}} \sqrt{1 + \left(\frac{\partial \bar{Z}}{\partial \bar{Y}}\right)^2} d\bar{Y}$$

$$\begin{aligned}
 &= \int_0^{\bar{Y}} \sqrt{1 + (a_3 + a_5\bar{X} + 2a_6\bar{Y})} \, d\bar{Y} \\
 &= \left(\frac{a_3 + a_5\bar{X}}{4a_6} + \frac{\bar{Y}}{2} \right) \cdot \sqrt{1 + (a_3 + a_5\bar{X} + 2a_6\bar{Y})^2} + \frac{\operatorname{arcsinh}(a_3 + a_5\bar{X} + 2a_6\bar{Y})}{4a_6} \quad (8)
 \end{aligned}$$

Similarly, the local displacements are obtained from,

$$\begin{Bmatrix} \bar{U} \\ \bar{V} \\ \bar{W} \end{Bmatrix} = \bar{T}^c \begin{Bmatrix} U \\ V \\ W \end{Bmatrix} \quad (9)$$

where,

$$\bar{T}^c = \begin{bmatrix} \frac{1}{\sqrt{1+(\frac{\partial \bar{Z}}{\partial \bar{X}})^2}} & 0 & \frac{-\frac{\partial \bar{Z}}{\partial \bar{X}}}{\sqrt{1+(\frac{\partial \bar{Z}}{\partial \bar{X}})^2}} \\ 0 & \frac{1}{\sqrt{1+(\frac{\partial \bar{Z}}{\partial \bar{Y}})^2}} & \frac{-\frac{\partial \bar{Z}}{\partial \bar{Y}}}{\sqrt{1+(\frac{\partial \bar{Z}}{\partial \bar{Y}})^2}} \\ \frac{\frac{\partial \bar{Z}}{\partial \bar{X}}}{\sqrt{1+(\frac{\partial \bar{Z}}{\partial \bar{X}})^2}} & \frac{\frac{\partial \bar{Z}}{\partial \bar{Y}}}{\sqrt{1+(\frac{\partial \bar{Z}}{\partial \bar{Y}})^2}} & \frac{1}{\sqrt{1+(\frac{\partial \bar{Z}}{\partial \bar{X}})^2+(\frac{\partial \bar{Z}}{\partial \bar{Y}})^2}} \end{bmatrix}. \quad (10)$$

then,

$$\begin{Bmatrix} U_i \\ V_i \\ W_i \end{Bmatrix} = [\Lambda_r]^{-1} \cdot [\bar{T}^c]_i^{-1} \begin{Bmatrix} u_i \\ v_i \\ w_i \end{Bmatrix} = [T_g]_i \cdot \begin{Bmatrix} u_i \\ v_i \\ w_i \end{Bmatrix} \quad (11)$$

such that the final transformation matrix is,

$$[T_G] = \begin{bmatrix} [T_g]_1 & 0 & 0 & 0 & 0 & 0 \\ 0 & [T_g]_2 & 0 & 0 & 0 & 0 \\ 0 & 0 & [T_g]_3 & 0 & 0 & 0 \\ 0 & 0 & 0 & [T_g]_4 & 0 & 0 \\ 0 & 0 & 0 & 0 & [T_g]_5 & 0 \\ 0 & 0 & 0 & 0 & 0 & [T_g]_6 \end{bmatrix} \quad (12)$$

acting on $\{u_1 \ v_1 \ w_1 \ u_2 \ v_2 \ w_2 \ u_3 \ v_3 \ w_3 \ u_4 \ v_4 \ w_4 \ u_5 \ v_5 \ w_5 \ u_6 \ v_6 \ w_6 \}$ and in which $[T_g]_i = [\Lambda_r]^{-1} \cdot [T_c]_i^{-1}$.

3.2 Element curvatures

Element curvatures in each element are defined with respect to the local flat plane co-ordinate system \bar{X} , \bar{Y} , \bar{Z} . With the out-of-plane geometry of the 6-node triangular element written as $\bar{Z} = f(\bar{X}, \bar{Y})$, then the curvatures about the local \bar{X} and \bar{Y} axes, are,

$$K_{\bar{X}} = -\frac{\partial^2 \bar{Z}}{\partial \bar{X}^2}, K_{\bar{Y}} = -\frac{\partial^2 \bar{Z}}{\partial \bar{Y}^2}, \quad (13)$$

and the torsion in the $\bar{X}\bar{Y}$ plane is,

$$K_{\bar{X}\bar{Y}} = -\frac{\partial^2 \bar{Z}}{\partial \bar{X} \partial \bar{Y}} \quad (14)$$

3.3 Relationship between out-of-plane force vector and element curvatures

The curvatures and stresses are combined to provide contributions to the out-of-plane nodal force vector components, per unit volume, as in,

$$\Delta f_{\bar{Z}} = K_{\bar{X}} \times \sigma_{\bar{X}} + K_{\bar{Y}} \times \sigma_{\bar{Y}} + K_{\bar{X}\bar{Y}} \times \tau_{\bar{X}\bar{Y}} = \{K_{\bar{X}} \quad K_{\bar{Y}} \quad K_{\bar{X}\bar{Y}}\} \begin{Bmatrix} \sigma_{\bar{X}} \\ \sigma_{\bar{Y}} \\ \tau_{\bar{X}\bar{Y}} \end{Bmatrix} \quad (15)$$

$$= [C_v] \cdot \{\sigma\} \quad (16)$$

where, $[C_v] = [K_{\bar{X}} \quad K_{\bar{Y}} \quad K_{\bar{X}\bar{Y}}]$ and $\{\sigma\} = \{\sigma_{\bar{X}} \quad \sigma_{\bar{Y}} \quad \tau_{\bar{X}\bar{Y}}\}^T$.

The out-of-plane forces (per unit volume) are subsequently transformed into nodal forces by integrating through the volume in the derivation of the equivalent nodal load vector (Eqn.29). The stiffness contribution arising from the curvatures are, therefore, introduced through the stresses induced by $\Delta f_{\bar{Z}}$ via the geometric stiffness matrix. This approach circumvents the need to introduce additional rotational degrees-of-freedom.

From Eqn. 15, it is apparent that if the element curvatures (Eqn 13) are zero, e.g. a flat surface, then $\Delta f_{\bar{Z}}$ is zero. In this case, the out-of-plane stiffness of the membrane relies purely on prestress. However, as the curvature increases, its effect is introduced through the standard Green's strain (e.g. see 20) and through the stress effects via $\Delta f_{\bar{Z}}$.

4 Strain-displacement relations

Nodal co-ordinates in local curved co-ordinate system are defined in the section 3. The area coordinate system(ξ_1, ξ_2, ξ_3 ; Fig.5), is defined for the six node curved triangular element, by the shape functions,

$$\begin{aligned}
 N_1 &= \xi_1(2\xi_1 - 1), & N_2 &= \xi_2(2\xi_2 - 1), \\
 N_3 &= \xi_3(2\xi_3 - 1), & N_4 &= 4\xi_1\xi_2, & N_5 &= 4\xi_2\xi_3, & N_6 &= 4\xi_3\xi_1
 \end{aligned}
 \tag{17}$$

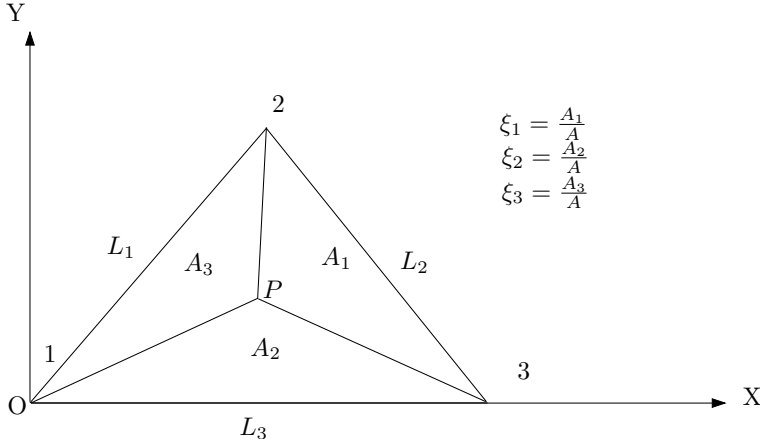


Figure 5: Area coordinate system

The displacement fields are approximated by,

$$U(X, Y) = \sum_{i=1}^6 N_i U_i, \quad V(X, Y) = \sum_{i=1}^6 N_i V_i, \quad W(X, Y) = \sum_{i=1}^6 N_i W_i
 \tag{18}$$

with the cartesian co-ordinates X and Y of the unstrained initial configuration approximated by,

$$X = \sum_{i=1}^6 N_i X_i, \quad Y = \sum_{i=1}^6 N_i Y_i,
 \tag{19}$$

in which, U_i, V_i, W_i and X_i, Y_i are nodal displacements and nodal co-ordinates respectively.

Surface strains are obtained from Green's definition as,

$$\begin{aligned}
 \boldsymbol{\varepsilon} &= \begin{Bmatrix} \varepsilon_X \\ \varepsilon_Y \\ \gamma_{XY} \end{Bmatrix} \\
 &= \begin{Bmatrix} \frac{\partial U}{\partial X} \\ \frac{\partial V}{\partial Y} \\ \frac{\partial V}{\partial X} + \frac{\partial U}{\partial Y} \end{Bmatrix} + \frac{1}{2} \cdot \begin{Bmatrix} \left(\frac{\partial U}{\partial X}\right)^2 + \left(\frac{\partial V}{\partial X}\right)^2 + \left(\frac{\partial W}{\partial X}\right)^2 \\ \left(\frac{\partial U}{\partial Y}\right)^2 + \left(\frac{\partial V}{\partial Y}\right)^2 + \left(\frac{\partial W}{\partial Y}\right)^2 \\ 2 \cdot \left\{ \frac{\partial U}{\partial X} \cdot \frac{\partial V}{\partial Y} + \frac{\partial V}{\partial X} \cdot \frac{\partial V}{\partial Y} + \frac{\partial W}{\partial X} \cdot \frac{\partial W}{\partial Y} \right\} \end{Bmatrix} \\
 &= \boldsymbol{\varepsilon}_L + \boldsymbol{\varepsilon}_{NL}
 \end{aligned} \tag{20}$$

with the component terms obtained from terms of the type,

$$\frac{\partial U}{\partial X} = \sum_{i=1}^6 \frac{\partial N_i}{\partial X} \cdot U_i, \text{ with } \frac{\partial N_i}{\partial X} = \sum_{i=1}^3 \frac{\partial N_i}{\partial \xi_i} \cdot \frac{\partial \xi_i}{\partial X} \quad \text{and,} \tag{21}$$

$$\begin{aligned}
 \frac{\partial \xi_1}{\partial X} &= \frac{Y_{23}}{2A}, & \frac{\partial \xi_2}{\partial X} &= \frac{Y_{31}}{2A}, \\
 \frac{\partial \xi_3}{\partial X} &= \frac{Y_{12}}{2A}, & \frac{\partial \xi_1}{\partial Y} &= \frac{X_{32}}{2A}, & \frac{\partial \xi_2}{\partial Y} &= \frac{X_{13}}{2A}, & \frac{\partial \xi_3}{\partial Y} &= \frac{X_{21}}{2A}
 \end{aligned} \tag{22}$$

where $2A = \det[A] = X_{21}Y_{31} - X_{31}Y_{21}$, and, $Y_{23} = Y_2 - Y_3$, etc., such that, for example,

$$\begin{aligned}
 \frac{\partial}{\partial X} U(X, Y) &= U_1 \frac{Y_{23}}{2A} (4\xi_1 - 1) + U_2 \frac{Y_{31}}{2A} (4\xi_2 - 1) \\
 &+ U_3 \frac{Y_{12}}{2A} (4\xi_3 - 1) + U_4 \frac{1}{2A} 4(\xi_2 Y_{23} + \xi_1 Y_{31}) \\
 &+ U_5 \frac{1}{2A} 4(\xi_3 Y_{31} + \xi_2 Y_{12}) + U_6 \frac{1}{2A} 4(\xi_1 Y_{12} + \xi_3 Y_{23}).
 \end{aligned} \tag{23}$$

5 Statements of Equilibrium

A virtual displacement δd is defined at the nodes, leading to virtual displacements and strains within the element of,

$$\delta u = N \delta d \quad \text{and} \quad \delta \boldsymbol{\varepsilon} = B \delta d, \tag{24}$$

respectively. The work done by the nodal forces,

$$\delta d^T \cdot f \tag{25}$$

Similarly, the internal work per unit volume done by the stresses δ , the curvature-induced out-of-plane force (Eqn. 15), and distributed forces, are,

$$\delta \varepsilon^T \cdot \sigma + \delta d \cdot \Delta f_{\bar{z}} - \delta u^T \cdot b, \text{ or, } \delta d(B^T \cdot \sigma + C_v \cdot \sigma - N^T \cdot b), \tag{26}$$

in which $b = \begin{Bmatrix} b_x \\ b_y \end{Bmatrix}$ is the distributed load, and b_x, b_y are the corresponding "body force" components.

Equating the external and internal work integrated over the volume of the element, V^e , then,

$$\delta d^T \cdot f = \delta d \left(\int_{V^e} (B^T + C_v) \sigma \, dV - \int_{V^e} N^T b \, dV \right), \text{ or,} \tag{27}$$

$$f = \int_{V^e} (B^T + C_v) \sigma \, dV - \int_{V^e} N^T b \, dV \tag{28}$$

Assuming linear elasticity defined by the elasticity matrix E , and a prestress, σ_0 , and negligible body forces, then,

$$f = \int_{V^e} (B^T + C_v) \cdot E \cdot B \cdot d \, dV + \int_{V^e} C_v \cdot \sigma_0 \, dV + \int_{V^e} B^T \cdot \sigma_0 \, dV, \tag{29}$$

in which,

$$B = B_0 + B_L \tag{30}$$

is the strain-displacement matrix noted in Eqn.20, decomposed into independent (B_0) and dependent (B_L) terms with respect to displacement. The contribution of the curvatures can be recognised in the first and second terms of Eqn. 29.

The components of B_0 can be obtained directly from the first term of Eqn.20 with, for example, Eqn.23. In obtaining the terms of B_{NL} it is convenient to write,

$$\begin{aligned}
\epsilon_{NL} &= \frac{1}{2} \begin{bmatrix} \frac{\partial U}{\partial X} & \frac{\partial V}{\partial X} & \frac{\partial W}{\partial X} & 0 & 0 & 0 \\ 0 & 0 & 0 & \frac{\partial U}{\partial Y} & \frac{\partial V}{\partial Y} & \frac{\partial W}{\partial Y} \\ \frac{\partial U}{\partial Y} & \frac{\partial V}{\partial Y} & \frac{\partial W}{\partial Y} & \frac{\partial U}{\partial X} & \frac{\partial V}{\partial X} & \frac{\partial W}{\partial X} \end{bmatrix} \cdot \begin{Bmatrix} \frac{\partial U}{\partial X} \\ \frac{\partial V}{\partial X} \\ \frac{\partial W}{\partial X} \\ \frac{\partial U}{\partial Y} \\ \frac{\partial V}{\partial Y} \\ \frac{\partial W}{\partial Y} \end{Bmatrix} = \frac{1}{2} A \cdot \begin{Bmatrix} \frac{\partial U}{\partial X} \\ \frac{\partial V}{\partial X} \\ \frac{\partial W}{\partial X} \\ \frac{\partial U}{\partial Y} \\ \frac{\partial V}{\partial Y} \\ \frac{\partial W}{\partial Y} \end{Bmatrix} \\
&= \frac{1}{2} A \cdot \Delta = \frac{1}{2} A \cdot G \cdot d = B_{NL} \cdot d, \tag{31}
\end{aligned}$$

where $d = \{U_1 \ V_1 \ W_1 \ U_2 \ V_2 \ W_2 \ U_3 \ V_3 \ W_3 \ U_4 \ V_4 \ W_4 \ U_5 \ V_5 \ W_5 \ U_6 \ V_6 \ W_6\}$ and G is a 6×18 matrix with non-zero terms,

$$\begin{aligned}
G_{1,1} &= \frac{Y_{23}}{2A}(4\xi_1 - 1), \quad G_{1,4} = \frac{Y_{31}}{2A}(4\xi_2 - 1), \quad G_{1,7} = \frac{Y_{12}}{2A}(4\xi_3 - 1) \\
G_{1,10} &= \frac{2}{A}(\xi_2 Y_{23} + \xi_1 Y_{31}), \quad G_{1,13} = \frac{2}{A}(\xi_3 Y_{31} + \xi_2 Y_{12}), \quad G_{1,16} = \frac{2}{2A}(\xi_1 Y_{12} + \xi_3 Y_{23}) \\
G_{2,2} &= \frac{Y_{23}}{2A}(4\xi_1 - 1), \quad G_{2,5} = \frac{Y_{31}}{2A}(4\xi_2 - 1), \quad G_{2,8} = \frac{Y_{12}}{2A}(4\xi_3 - 1) \\
G_{2,11} &= \frac{2}{A}(\xi_2 Y_{23} + \xi_1 Y_{31}), \quad G_{2,14} = \frac{2}{A}(\xi_3 Y_{31} + \xi_2 Y_{12}), \quad G_{2,17} = \frac{2}{2A}(\xi_1 Y_{12} + \xi_3 Y_{23}) \\
G_{3,3} &= \frac{Y_{23}}{2A}(4\xi_1 - 1), \quad G_{3,6} = \frac{Y_{31}}{2A}(4\xi_2 - 1), \quad G_{3,9} = \frac{Y_{12}}{2A}(4\xi_3 - 1) \\
G_{3,12} &= \frac{2}{A}(\xi_2 Y_{23} + \xi_1 Y_{31}), \quad G_{3,15} = \frac{2}{A}(\xi_3 Y_{31} + \xi_2 Y_{12}), \quad G_{3,18} = \frac{2}{2A}(\xi_1 Y_{12} + \xi_3 Y_{23}) \\
G_{4,1} &= \frac{X_{32}}{2A}(4\xi_1 - 1), \quad G_{4,4} = \frac{X_{13}}{2A}(4\xi_2 - 1), \quad G_{4,7} = \frac{X_{21}}{2A}(4\xi_3 - 1) \\
G_{4,10} &= \frac{2}{A}(\xi_2 X_{32} + \xi_1 X_{13}), \quad G_{4,13} = \frac{2}{A}(\xi_3 X_{13} + \xi_2 X_{21}), \quad G_{4,16} = \frac{2}{2A}(\xi_1 X_{21} + \xi_3 X_{32}) \\
G_{5,2} &= \frac{X_{32}}{2A}(4\xi_1 - 1), \quad G_{5,5} = \frac{X_{13}}{2A}(4\xi_2 - 1), \quad G_{5,8} = \frac{X_{21}}{2A}(4\xi_3 - 1) \\
G_{5,11} &= \frac{2}{A}(\xi_2 X_{32} + \xi_1 X_{13}), \quad G_{5,14} = \frac{2}{A}(\xi_3 X_{13} + \xi_2 X_{21}), \quad G_{5,17} = \frac{2}{2A}(\xi_1 X_{21} + \xi_3 X_{32}) \\
G_{6,3} &= \frac{X_{32}}{2A}(4\xi_1 - 1), \quad G_{6,6} = \frac{X_{13}}{2A}(4\xi_2 - 1), \quad G_{6,9} = \frac{X_{21}}{2A}(4\xi_3 - 1) \\
G_{6,12} &= \frac{2}{A}(\xi_2 X_{32} + \xi_1 X_{13}), \quad G_{6,15} = \frac{2}{A}(\xi_3 X_{13} + \xi_2 X_{21}), \quad G_{6,18} = \frac{2}{2A}(\xi_1 X_{21} + \xi_3 X_{32}). \tag{32}
\end{aligned}$$

The resulting expressions comprising B_{NL} are somewhat cumbersome. An indication of the nature of these terms is given, for example, by,

$$\begin{aligned}
 B_{1,1} = & \frac{Y_{23}}{2A}(4\xi_1 - 1) + U_1 \frac{Y_{23}^2}{8A^2}(4\xi_1 - 1)^2 + \frac{Y_{23}}{2A}(4\xi_1 - 1)[U_2 \frac{Y_{31}}{2A}(4\xi_2 - 1) \\
 & + U_3 \frac{Y_{12}}{2A}(4\xi_3 - 1) + U_4 \frac{4}{2A}(\xi_2 Y_{23} + \xi_1 Y_{31}) + U_5 \frac{4}{2A}(\xi_3 Y_{31} + \xi_2 Y_{12}) \\
 & + U_6 \frac{4}{2A}(\xi_1 Y_{12} + \xi_3 Y_{23})]. \tag{33}
 \end{aligned}$$

If the initial stress vector is,

$$\sigma_0 = \begin{Bmatrix} \sigma_{X0} \\ \sigma_{Y0} \\ \tau_{XY0} \end{Bmatrix}, \tag{34}$$

then,

$$\begin{aligned}
 A^T \cdot \sigma_0 = & \begin{bmatrix} \frac{\partial U}{\partial X} & 0 & \frac{\partial U}{\partial Y} \\ \frac{\partial V}{\partial X} & 0 & \frac{\partial V}{\partial Y} \\ \frac{\partial W}{\partial X} & 0 & \frac{\partial W}{\partial Y} \\ 0 & \frac{\partial U}{\partial Y} & \frac{\partial U}{\partial X} \\ 0 & \frac{\partial V}{\partial Y} & \frac{\partial V}{\partial X} \\ 0 & \frac{\partial W}{\partial Y} & \frac{\partial W}{\partial X} \end{bmatrix} \cdot \begin{Bmatrix} \sigma_{X0} \\ \sigma_{Y0} \\ \tau_{XY0} \end{Bmatrix} \\
 = & \begin{Bmatrix} \frac{\partial U}{\partial X} \cdot \sigma_{X0} + \frac{\partial U}{\partial Y} \cdot \tau_{XY0} \\ \frac{\partial V}{\partial X} \cdot \sigma_{X0} + \frac{\partial V}{\partial Y} \cdot \tau_{XY0} \\ \frac{\partial W}{\partial X} \cdot \sigma_{X0} + \frac{\partial W}{\partial Y} \cdot \tau_{XY0} \\ \frac{\partial U}{\partial Y} \cdot \sigma_{Y0} + \frac{\partial U}{\partial X} \cdot \tau_{XY0} \\ \frac{\partial V}{\partial Y} \cdot \sigma_{Y0} + \frac{\partial V}{\partial X} \cdot \tau_{XY0} \\ \frac{\partial W}{\partial Y} \cdot \sigma_{Y0} + \frac{\partial W}{\partial X} \cdot \tau_{XY0} \end{Bmatrix} \tag{35}
 \end{aligned}$$

$$= \begin{bmatrix} \sigma_{X0} & 0 & 0 & \tau_{XY} & 0 & 0 \\ 0 & \sigma_{X0} & 0 & 0 & \tau_{XY} & 0 \\ 0 & 0 & \sigma_{X0} & 0 & 0 & \tau_{XY} \\ \tau_{XY} & 0 & 0 & \sigma_{Y0} & 0 & 0 \\ 0 & \tau_{XY} & 0 & 0 & \sigma_{Y0} & 0 \\ 0 & 0 & \tau_{XY} & 0 & 0 & \sigma_{Y0} \end{bmatrix} \cdot \begin{Bmatrix} \frac{\partial U}{\partial X} \\ \frac{\partial V}{\partial X} \\ \frac{\partial W}{\partial X} \\ \frac{\partial U}{\partial Y} \\ \frac{\partial V}{\partial Y} \\ \frac{\partial W}{\partial Y} \end{Bmatrix} \tag{36}$$

$$= M \cdot \Delta, \tag{37}$$

in which,

$$M = \begin{bmatrix} \sigma_{X0}[I_3] & \tau_{XY0}[I_3] \\ \tau_{XY0}[I_3] & \sigma_{Y0}[I_3] \end{bmatrix}.$$

In defining $\varepsilon_{NL} = B_L \cdot d$ (Eqn. 31), then

$$\varepsilon_{NL}^T \cdot \sigma_0 = d^T \cdot B_L^T \cdot \sigma_0. \tag{38}$$

Noting from Eqn.31 that $\varepsilon_{NL} = \frac{1}{2}A \cdot G \cdot d$, and substituting this into Eqn. 38, then,

$$\begin{aligned} \text{or, } & \left(\frac{1}{2}A \cdot G \cdot d\right)^T \cdot \sigma_0 = d^T \cdot B_L^T \cdot \sigma_0 \\ & \frac{1}{2} d^T \cdot G^T \cdot A^T \cdot \sigma_0 = d^T \cdot B_L^T \cdot \sigma_0. \end{aligned} \tag{39}$$

Using 35 and 37 with 31 such that,

$$A^T \cdot \sigma_0 = M \cdot \Delta = M \cdot G \cdot d,$$

then 39 becomes,

$$\begin{aligned} \text{or, } & \frac{1}{2} d^T \cdot G^T \cdot M \cdot G \cdot d = d^T \cdot B_L^T \cdot \sigma_0 \\ & \frac{1}{2} G^T \cdot M \cdot G \cdot d = B_L^T \cdot \sigma_0. \end{aligned} \tag{40}$$

Assuming zero body forces, then from Eqn. 28,

$$\int_{V^e} (B^T + C_v)\sigma - f = 0, \tag{41}$$

or,

$$f = \int_{V^e} (B^T + C_v)\sigma d V. \tag{42}$$

The out-of-balance force vector, denoted by ψ , can then be written as,

$$\psi(u) = \int_{V^e} (B^T + C_v)\sigma - F dV \quad (43)$$

where F is external force vector, and B is defined from the general strain definition,

$$d\varepsilon = Bdu.$$

If the element nodal displacements, u , are large, the strains depend non-linearly on displacements, such that,

$$B = B_0 + B_L(u).$$

Assuming reasonably small strains, then,

$$\sigma = E(\varepsilon - \varepsilon_0) + \sigma_0,$$

in which E is the usual set of elastic constants, then 43 becomes,

$$d\psi = \int_{V^e} dB^T + dC_v\sigma dV + \int_{V^e} (B^T + C_v) d\sigma = K_T \cdot du,$$

with $d\sigma = E \cdot d\varepsilon = E \cdot B \cdot du$, $dB = dB_L$ and $dC_v = 0$.

Therefore,

$$d\psi = \int_{V^e} dB_L^T \sigma \cdot dV + K_E \cdot du, \quad (44)$$

where,

$$K_E = \int_{V^e} (B^T + C_v)EB dV. \quad (45)$$

The first term can be generally written as,

$$\int_V dB_L^T \sigma dV = K_\sigma du, \quad (46)$$

where K_σ is a symmetric matrix dependent on the stress level and identified as the initial stress or geometric stiffness matrix. Therefore,

$$d\psi = (K_E + K_\sigma) \cdot du = K_T \cdot du. \quad (47)$$

6 Computational implementation

6.1 Numerical integration

As equations of the type Eqn.44 are relatively complex and difficult to integrate analytically, numerical integration techniques are used instead in the form of Gauss quadrature in which,

$$\int_{\Omega_V} \psi(\xi_{1i}, \xi_{i2}, \xi_{i3}) dV = \int_{\Omega_A} \phi(\xi_{1i}, \xi_{i2}, \xi_{i3}) dA = \frac{1}{2} \sum_{i=1}^n W_i J_i \phi_i \quad (48)$$

in which for example, ϕ_i and J_i are the values of ϕ and the Jacobian matrix J , calculated respectively at the specific sampling point location ξ_i with the corresponding weight factor W_i .

Area coordinates are not independent but must satisfy the constraint,

$$\xi_1 + \xi_2 + \xi_3 = 1. \quad (49)$$

We define:

$$\begin{aligned} \xi_1 &= \zeta \\ \xi_2 &= \eta \\ \xi_3 &= 1 - \zeta - \eta \end{aligned} \quad (50)$$

Normally if the shape function ψ is a polynomial, then integration using Eqn 48 can be achieved accurately with an adequate number of Gauss points based on the highest order terms of the function ψ . For the undistorted LST element, the Jacobian matrix $|J|$ is constant, making ψ a polynomial of order four, requiring six Gauss points for accurate integration.

However, geometric distortion produces a Jacobian matrix, $[J]$, whose terms are not simple polynomials but rather the ratio of two polynomials. Inexact integration is obtained using six Gauss points for elements with edges that are not straight and nodes that are not at the midpoints. Twelve Gauss points achieve the required level of accuracy without compromising computational efficiency.

Measures of these types of distortion have been proposed. For example, the mid-point coefficient μ , defined as the maximum distance from mid nodes to the middle position of the element side (Lo, S.H., (1985)), and the curvature coefficient β , which is a function of element shape factor and curvatures of the element sides, (Lo, S.H., (1989)). However, using the criterion that $|J| > 0$ at each and every

Gauss point clearly identifies the second shape as unacceptable from a computational perspective. The key advantage of using $|J|$ at each Gauss point to assess distortion is that the calculation carries no computational overhead since the determination of $|J|$ is required to calculate the element stiffness matrix and out-of-balance-force-vector. It also provides an unequivocal check no matter the type of distortion as clearly all values of $|J|$ at the Gauss points must be positive definite. This element check is used in the work described in this paper and is essential in the accurate calculation of membrane structure equilibrium and in contributing to numerical stability of the solution algorithm.

7 Solution Algorithm

The geometric nonlinearity associated with membrane structure analysis makes it necessary to adopt an iterative strategy to solve the equilibrium equations derived in section 5. In classic finite element non-linear analysis, it would be normal and expected to adopt the Newton-Raphson method. However, in fabric structure analysis where, for example, the continuum is represented by pseudo cables Barnes M.R., (1999), dynamic relaxation is normally used. Outcomes of the application of both solvers to the present element formulation are reported in this paper.

7.1 Dynamic relaxation algorithm

The Dynamic Relaxation algorithm is based on the principle that any body which is in motion will come to rest only when it is at a state of equilibrium. The system is forced into a pseudo oscillation, with equal amplitude about the equilibrium position. Both the frequency and the amplitude of the fictitious dynamic motion are controlled through the components of stiffness and of out-of-balance force at each node of the discretization, and by the associated nodal mass.

Kinetic Damping has been shown to be a more stable and a more rapidly convergent technique for damping the pseudo dynamic oscillations of the discretized system, when compared with the alternative viscous damping approach Barnes, M.R., (1980). Using this technique the system is permitted to vibrate freely without attenuation of displacement or frequency. During this motion the kinetic energy of the entire system is monitored. As the system passes the equilibrium configuration the kinetic energy of the system is maximized. When a maximum value is observed the current oscillation is halted. The pseudo motion is then restarted from this new configuration. As more peaks in the kinetic energy of the system are detected, the proximity of the system to the true equilibrium configuration is increased. The procedure culminates in the minimisation of the sum of the kinetic and potential

energies of the system at equilibrium.

The key advantage of the dynamic relaxation algorithm is that matrix operations are kept to a minimum along with storage requirements and data transfer is also small. However, the associated disadvantage is that by using only the diagonal stiffness terms there is a level of uncoupling that can lead to undesirable element distortion. For example, when loads are applied to the membrane, the solution algorithm results in some nodal displacements lagging behind neighbouring nodes (e.g. see fig. 6).

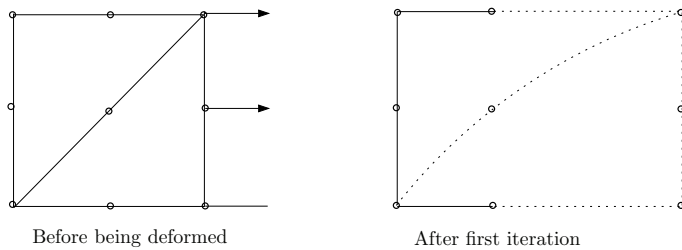


Figure 6: Element distortion associated with dynamic relaxation - coarse mesh (a) undeformed, (b) deformed.

With mesh refinement, the problem is compounded, as the distortion becomes more severe as the element size reduces (e.g. see figure 7). When a highly refined mesh is used, a smoothly convergent solution procedure is not guaranteed, and accurate results are only obtained when elements are not seriously distorted.

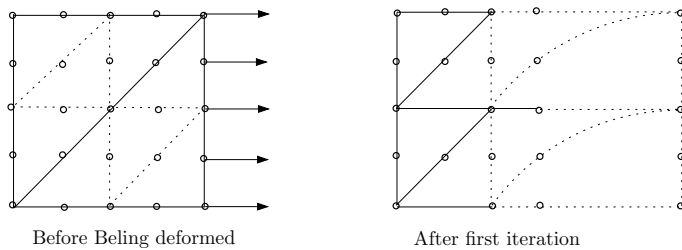


Figure 7: Element distortion associated with dynamic relaxation - refined mesh (a) undeformed, (b) deformed.

In the absence of geodesic strings, this problem may be solved by using a mesh-refinement procedure. Form-finding can start with a very coarse mesh, including

a small number of elements, whose sizes are comparatively large and unlikely to become too distorted. The mesh is refined by replacing each distorted element with several undistorted elements using the geometric configuration obtained from the preceding form-finding analysis. Form-finding and mesh-refinement are repeated until convergence.

7.2 Newton-Raphson (N-R) Method

The Newton-Raphson method is one of the most widely used and well known methods for solving nonlinear equations in which the first derivatives of the nonlinear function with respect to the variable are used to approach the root smoothly and quadratically. It is sufficient to state here that the standard N-R method is adopted with the tangent stiffness defined as,

$$\frac{dP}{du} = \frac{d}{du}(k_0u + k_{Nu}) = k_0 + \frac{d}{du}(k_{Nu}) = k_t, \quad (51)$$

where P is the out-of-balance force vector.

8 Wrinkling

With relatively negligible flexural stiffness, vanishing of tensile stresses in an arbitrary position or direction of the membrane surface will immediately lead to buckling in the form of wrinkles in the membrane material. In this case, the membrane will completely or partially lose stiffness and load resistance in the wrinkled area. From the perspective of either aesthetics or structural safety, wrinkling can be regarded as a type of structural (serviceability) failure, and should be inadmissible during membrane structural design. Structural analysis taking into account wrinkling is sophisticated because the detailed wrinkling pattern not only depends on the stress state but the imperfection of membrane material introduced during the fabrication process. Therefore, in this section, the main aim of the finite element formulation taking into account wrinkling concentrates on the prediction of wrinkling under loading as opposed to simulating the physical forms of the wrinkles.

Wrinkling criteria developed by Otto, F., (1962), Miller et al, (1985) and Rodde-
man, D.G., (1987) (summarised in Table 1) are based on principal stress (denoted σ_p), strain (ϵ_p) or combined principal strain and stress (σ_p, ϵ_p). According to these criteria, the membrane state can be described as taut(no wrinkle), wrinkled(uniaxial wrinkling) or slack (biaxial wrinkling).

Wrinkling criteria			Wrinkling Membrane	
σ_p	ε_p	σ_p, ε_p	state	state
$\sigma_{II} > 0$	$\varepsilon_I \geq 0$ and $\varepsilon_{II} \geq \nu \varepsilon_I$	$\sigma_{II} > 0$	None	Taut
$\sigma_I > 0$ and $\sigma_{II} < 0$	$\varepsilon_I \geq 0$ and $\varepsilon_{II} \leq -\nu \varepsilon_I$	$\varepsilon_I \geq 0$ and $\sigma_{II} \leq 0$	Uniaxial	Wrinkled
$\sigma_I \leq 0$	$\varepsilon_I \leq 0$	$\varepsilon_I \leq 0$	Biaxial	Slack

Table 1: Wrinkling criteria based on principal stresses

For the local stresses $\sigma_X, \sigma_Y, \tau_{XY}$, the major principal stress σ_I and minor principal stress σ_{II} are,

$$\sigma_{I,II} = \frac{\sigma_X + \sigma_Y}{2} \pm \sqrt{\left(\frac{\sigma_X - \sigma_Y}{2}\right)^2 + \tau_{XY}^2}, \quad (52)$$

and corresponding principal strains are,

$$\varepsilon_{I,II} = \frac{\varepsilon_X + \varepsilon_Y}{2} \pm \sqrt{\left(\frac{\varepsilon_X - \varepsilon_Y}{2}\right)^2 + \left(\frac{\gamma_{XY}}{2}\right)^2} \quad (53)$$

In zones where wrinkling occurs, the direction of the major principal strain (ε_I) is colinear with the wrinkle direction. If θ_p is the angle between wrinkle direction and local X axis, then,

$$\theta_p = \frac{1}{2} \tan^{-1} \left(\frac{2\gamma_{XY}}{\varepsilon_X - \varepsilon_Y} \right). \quad (54)$$

When calculating the element stiffness matrix, the existence of wrinkling should be taken into account. In this case it is not sufficient to use

$$\{\sigma\} = \{\sigma_X \quad \sigma_Y \quad \tau_{XY}\}^T = [E] \begin{Bmatrix} \varepsilon_X \\ \varepsilon_Y \\ \gamma_{XY} \end{Bmatrix} = [E][B]\{U\} \quad (55)$$

in which, $\{U\}$ is the vector of nodal displacements. If compressive stresses are not permitted and therefore the stiffness normal to the wrinkle direction is zero, solution convergence is not always smooth and sometimes may not be achieved Rossi, R., (2005); Liu, X., (2001); Rossi, R., (2003). Rossi Rossi, R., (2005) proposed an algorithm for the stabilization of the material manipulation. Using his method, if the membrane is in a "wrinkled state", a modified elastic stiffness matrix $[E_{mod}]$ is defined as,

$$[E_{mod}] = \begin{bmatrix} E_{rot,11} & P \cdot E_{rot,12} & E_{rot,13} \\ P \cdot E_{rot,21} & P \cdot E_{rot,22} & P \cdot E_{rot,23} \\ E_{rot,31} & P \cdot E_{rot,32} & E_{rot,33} \end{bmatrix} = [E_{rot}] \times [P] \quad (56)$$

in which, P is the penalization parameter, and,

$$[E_{rot}] = [R]^T [E] [R]. \quad (57)$$

$[R]$ is a transformation matrix. Denoting the orientation of the principal stress to the local X axis is α_w , then

$$c = \cos(\alpha_w); s = \sin(\alpha_w); [R] = \begin{bmatrix} c^2 & s^2 & -2cs \\ s^2 & c^2 & 2sc \\ sc & -sc & c^2 - s^2 \end{bmatrix} \quad (58)$$

If the penalization is constant, the performance of the wrinkling procedure may be compromised. An alternative definition of P to improve the stability is to make P a function of the maximum (σ_{max}) and effective compressive stresses (σ_2) Rossi, R., (2005),

$$P_\sigma = \frac{\sigma_{max}}{\sigma_2} \rightarrow \left\{ \begin{array}{ll} P_\sigma > P & \rightarrow P = P_\sigma \\ P_\sigma > 1 \text{ or } P_\sigma < 0 & \rightarrow P = 1.0 \end{array} \right\}. \quad (59)$$

If the modification makes the state change (from wrinkled or slack to taut), then P is increased by a factor ω , where $\omega = 10$ is recommended (Rossi, R., (2005)). The elastic stiffness matrix then becomes,

$$K_{E,mod} = \int_V B^T [E_{mod}] B dv \quad (60)$$

In addition to the obvious change in the element stiffness matrix, the equivalent nodal load vector is also changed to be of the form,

$$f_e = \int_V B_0 (E_{mod} \cdot \epsilon + \sigma_0) dV. \quad (61)$$

In this method, a small compressive stress is allowed in the analysis to enhance the stability of solution procedure and the accuracy. It is necessary to note that there it is not assured that the "fictitious" compressive stresses are removed during each iteration and at the final configuration, but wrinkling can be predicted with an acceptable accuracy and economical computational cost using this approach Rossi, R., (2005).

9 Numerical Examples

Unlike most finite element applications, benchmarks for membrane structure analysis have not commonly been proposed owing to the complexity of the geometry

and the influences of geometric non-linearities. In this section we present a number of example solutions that compare the present linear strain triangular element (LST) with solutions obtained from a constant strain triangle membrane formulation (CST), and a thin shell solution. We also demonstrate the capability of the formulation to predict wrinkling, and the efficiency of the proposed element when coupled with dynamic relaxation and Newton-Raphson solution strategies. Finally we include the analysis of an actual structure.

The constant strain triangle membrane formulations used as comparators in this section are based on a so-called cable analogy in which the continuum triangle is represented by three cables (or bars as compression is permitted). The stiffnesses (both elastic and geometric) and the forces in the representative cables are calculated so as to represent the strain and stress state within the continuum triangle. The membrane structure is then analysed as a cable network, in this case using dynamic relaxation. The small strains formulation is based on the application of the principle of calculation of strains at an inclined plane. In the large strain CST formulation, Green's strain links nodal displacements to strains. For both CST element types large deformations are assumed. Further details of the CST formulations and their specific relative merits can be found in Zhang, L., (2010).

9.1 *Hypar*

A typical saddle shape membrane supported by tensioned boundary cables shown in figure 8. A and B indicate two high points, with C and D the corresponding low points. The warp direction is aligned along the line AB, and fill direction is normal to the warp direction in the membrane element plane. The form-finding stage of the analysis is originated from a shape made of two flat planes as shown in figure 9(a). The resulting equilibrated and prestressed geometry is a hypar, indicated in figure 9(b) and the form-finding results using 256 CST elements and 128 LST elements are illustrated in Fig.10 and Fig.11.

A uniform load $N = 1kN/m^2$ is applied to the hypar membrane in the z direction (defined in figure 8). Figures 12-14 comparatively illustrate the membrane stress distributions using 256 large strain CST elements, and 128 large strain LST finite elements. The shear stresses shown in figure 14 are the absolute values, recognizing that the positive and negative shear stresses represent the shear forces in clockwise and anticlockwise directions separately. The same stress ranges are used for the CST and LST results to enable direct visual comparison.

Both CST and LST formulations predict that, in the warp direction, the membrane stresses decrease from two low points C,D to the symmetrical axis across two high points A,B (figures 12-14). Conversely in the fill direction, the stresses increase

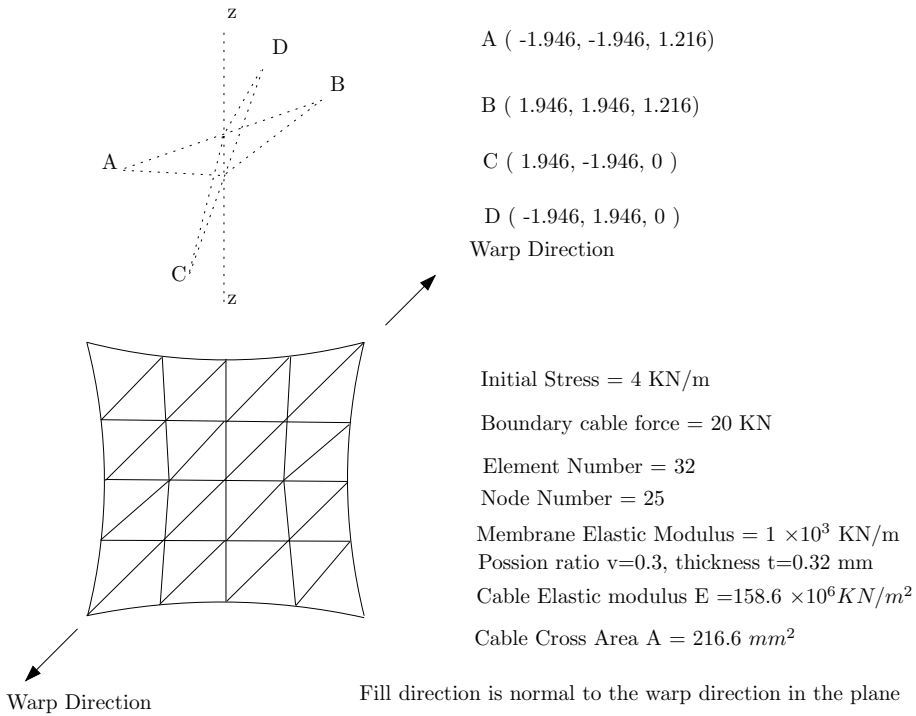


Figure 8: A Saddle membrane supported by boundary cables

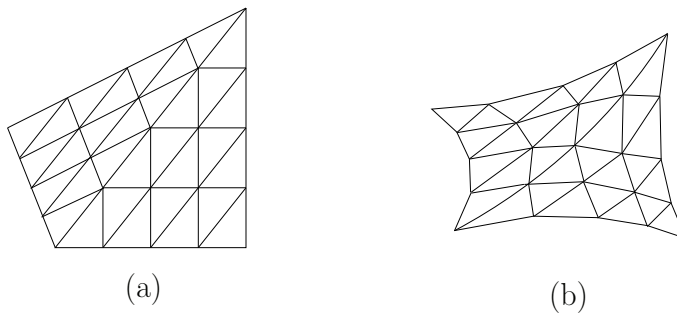


Figure 9: Initial and balanced geometry with initial stress $\sigma_x = \sigma_y = 4kN/m$ and boundary cable forces $N = 20kN$

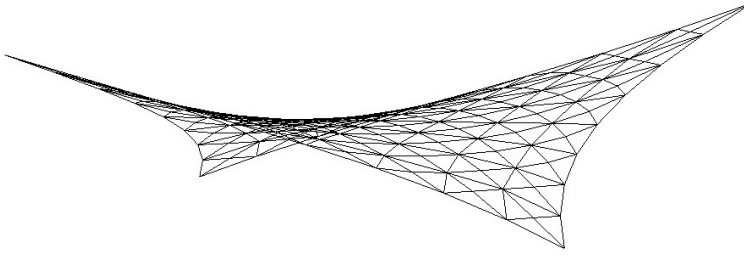


Figure 10: Formfinding of the Hypar membrane using 256 CST elements

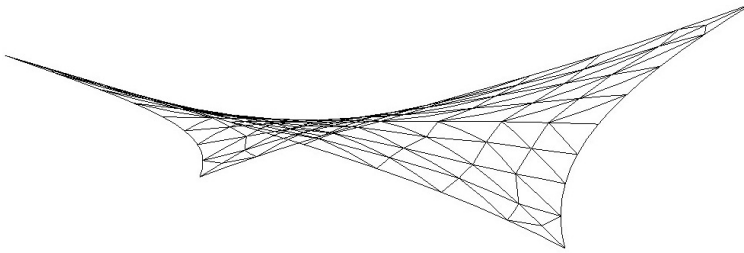


Figure 11: Formfinding of the Hypar membrane using 128 LST elements

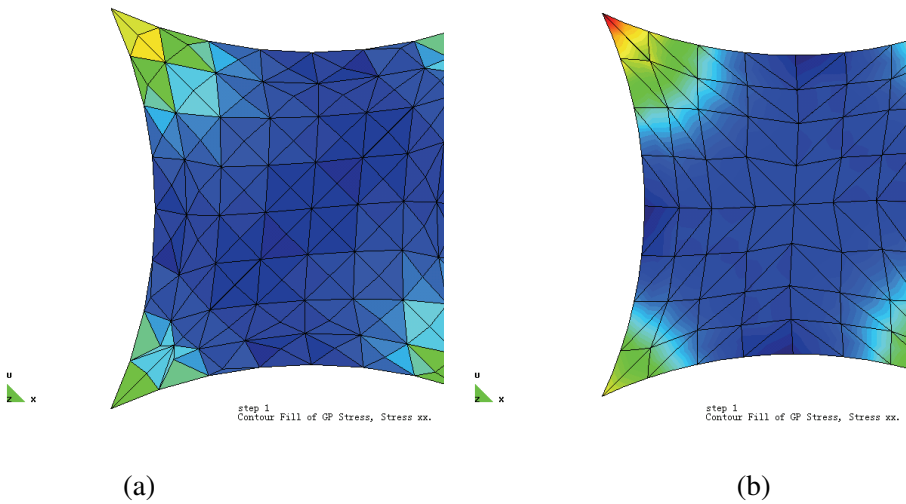


Figure 12: Stress along the warp direction — (a) CST, (b) LST

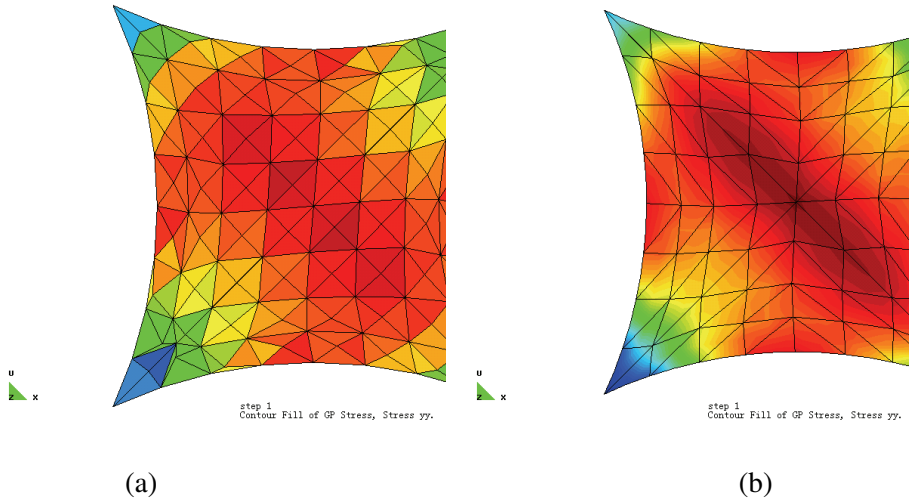


Figure 13: Stress along the fill direction — (a) CST, (b) LST

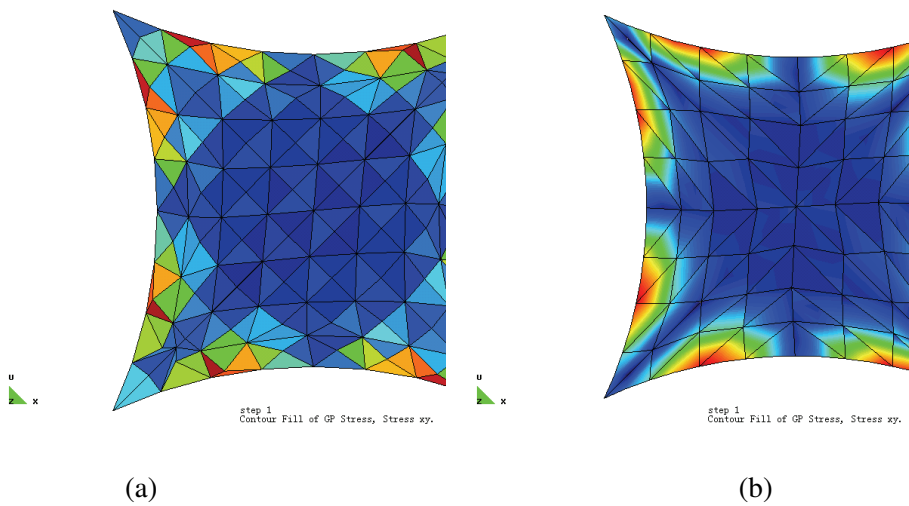


Figure 14: Shear stress across the warp and fill direction — (a) CST, (b) LST

from the two low points A,B to the symmetrical axis across C,D. The shear stresses are generally uniformly distributed and close to zero. Pockets of shear stress appear at points along the boundary cables. The ranges of the membrane stress obtained from CST (large strain) and LST models (warp stresses are illustrated in fig. 15 as an example) converge to similar values.

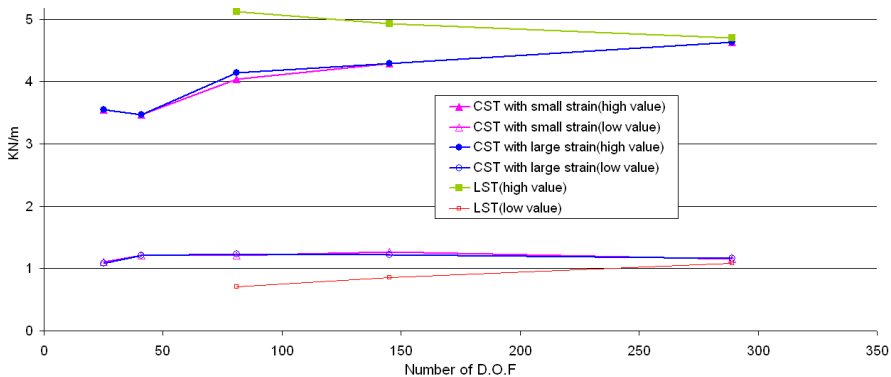


Figure 15: Warp stress as a function of the number of D.O.F

Similar convergence properties are displayed when predicting the deflected shape of the membrane. For example, the central node displacement is shown in fig. 16 as a function of numbers of degrees-of-freedom (DOF), although it is interesting to note that convergence is from opposite sides of the stabilised solution.

When subjected to an upwards load, the membrane stresses in the central area increase along the fill direction and decrease along the warp direction. In contrast, the membrane stresses near the fixed points increase along the warp direction and decrease along the fill direction (figure 12 and 13). This stress pattern results from the integrated structural response of membrane surface and boundary cables near the boundary area, where membrane stress is associated with the deformation of both membrane and boundary cable elements. With the narrowing of the fabric in these regions, the effect from cable elements is more pronounced. For example, near the low points, even with reduced curvature along warp direction of membrane surface, the enhanced membrane stress along the warp direction is dominated by the stretching and deformation of the boundary cables.

It is notable that the membrane stresses along warp direction represented by LST (Fig. 12) change rapidly near the two low points of the hyper. Whilst even with same D.O.F as figure 17, such detailed information of membrane stress in that area is less easy to obtain using large strain CST (e.g. figure 12), since the membrane

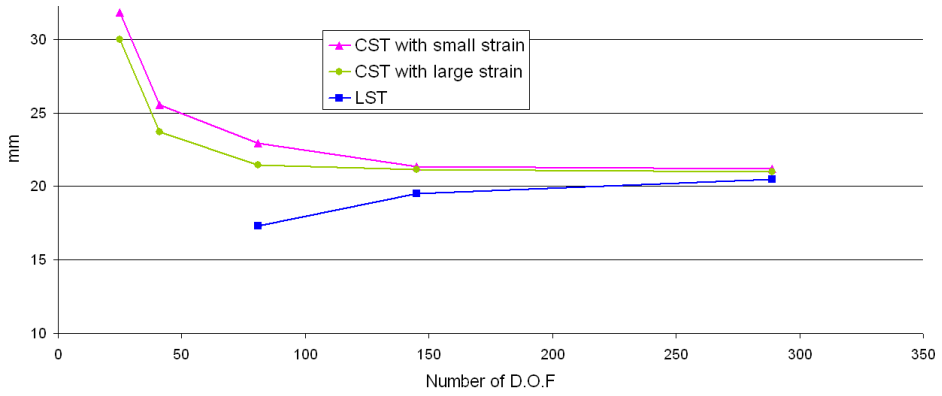


Figure 16: Central node displacement as a function of the number of D.O.F. Number

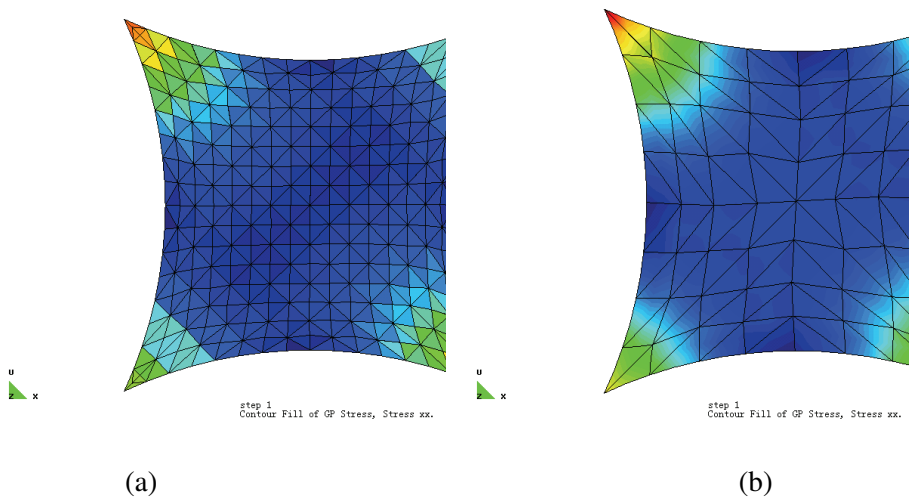


Figure 17: Stress along warp direction - (a) CST with refined mesh, (b) LST

stress of interest is constant across every element in the CST. Therefore, a refined mesh is required to enable CST to provide a more accurate estimate of the structure response. An indication of any required mesh refinement is obviously only obtained after an initial analysis. Whilst stress gradients with a LST at the element boundaries can be used to imply adequacy of the mesh density, it is more difficult to demonstrate convergence with the CST.

9.2 Predicting membrane wrinkling - shear test demonstration

To demonstrate the capabilities of the developed wrinkling criterion (stress-strain combined) and calculation algorithm, a reference shear test Ishii, K., (1989) is defined as in fig. 18. In the physical shear test the membrane is initially pre-stressed in the x-direction by a displacement of $u_x = 1\text{mm}$. This displacement is held fixed for the subsequent shear loading inducing by a displacement, u_y in the range $0 - 10\text{mm}$. An isotropic ET-foil membrane material is assumed (ET-foil thickness $t = 200\mu$, Young's modulus is $E = 600\text{N}/\text{mm}^2$ and the Poisson's ratio $\mu = 0.45$).

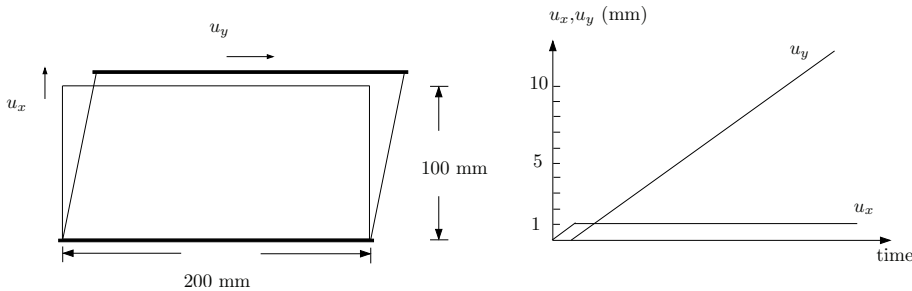


Figure 18: Geometry, boundary and loading conditions for the shear test calculation

The corresponding numerical results from reference Ishii, K., (1989) are shown in fig. 19, in which, u_x and u_y denote the orthogonal displacements in the membrane plane respectively, and u_z reflects the depth of the wrinkles in the membrane.

As presented in fig. 19, the wrinkles start to appear at the two ends, then propagate to the middle of the patch. It is also observed that wrinkling develops before the lateral displacement u_y reaches 1.65mm , with the wrinkle depths u_z less than 0.0035mm . From $u_y = 1.65\text{mm}$ the wrinkles start to develop with increased frequency, and the maximum wrinkle depth increases up to 0.62mm for a small increment ($\Delta u_y = 2.0 - 1.65 = 0.35\text{mm}$) in the lateral displacement. After $u_y = 2.0\text{mm}$, the wrinkles develop proportionally, and propagate to the majority of the foil at $u_y = 2.2\text{mm}$.

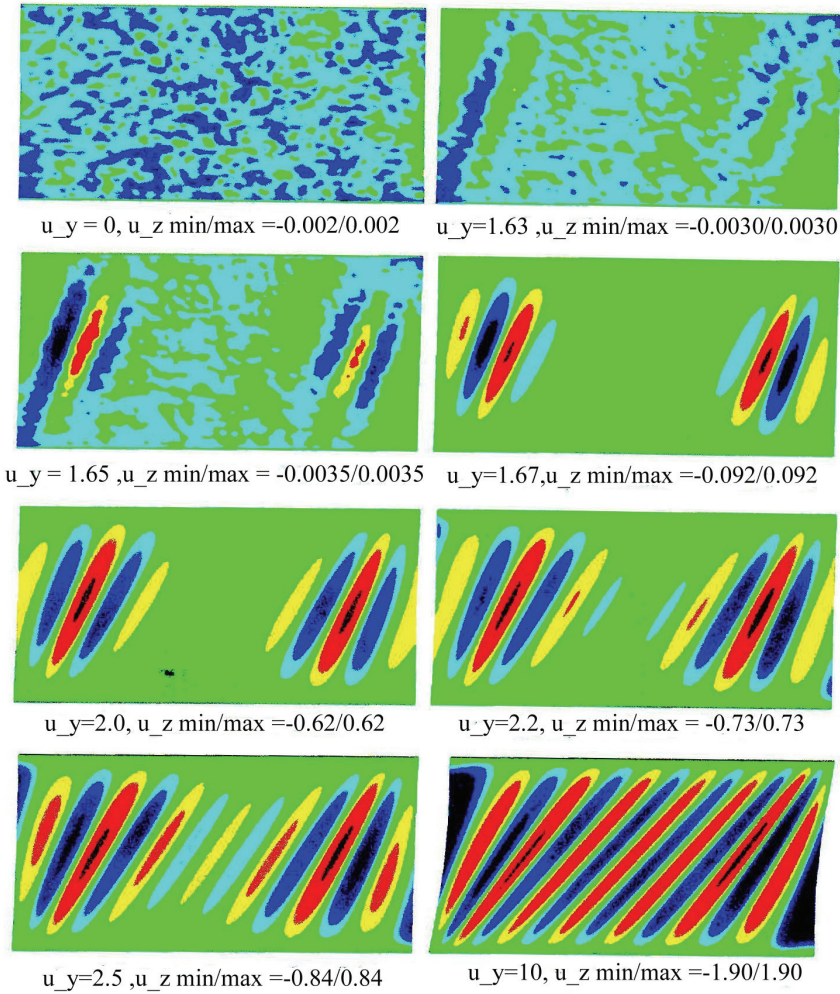


Figure 19: Displacement u_z [mm] normal to the membrane plane for the development of wrinkles for selected shear displacements u_y in reference test

The shear test is simulated using 16 LST elements (fig. 20). The element mesh is coarse compared to the mesh used in the reference solution Ishii, K., (1989) (at least 10×20) which aimed at determining the details of the wrinkles (e.g depths) using hexahedral elements. It is notable that in the reliability analysis of fabric structures using membrane finite elements, wrinkling is regarded as one of the structural failure modes, with the main target to predict the onset and existence of wrinkles

accurately and immediately, and not necessarily the wrinkle details. For this reason it is undesirable to use a dense mesh to assess the LST element capabilities in predicting wrinkling based on the criterion and the algorithm described in section 8.

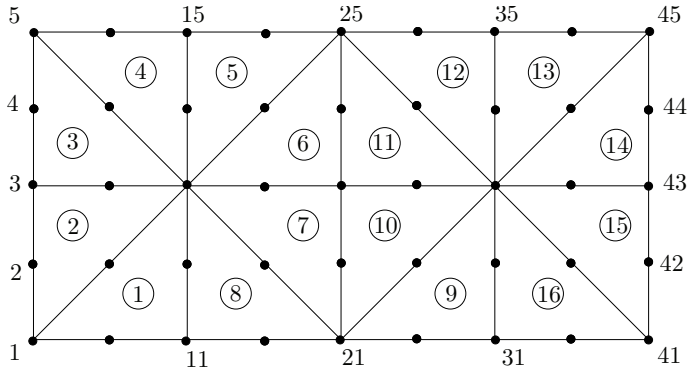


Figure 20: LST F.E Mesh for the wrinkle patch

The predicted positions and their directions of wrinkles are presented in fig. 21 with the dash-lines representing the wrinkles, with their directions. The existence of wrinkles and directions are assessed and calculated based on the principal stresses at the twelve element Gauss points, the positions of which have been described in section 6. Wrinkling information may, therefore, be provided at each Gauss point.

Comparison of figs. 21 with fig. 19, suggests that the existence of wrinkling in the patch can be accurately predicted by the LST formulation, even when they are not easy to observe in three-dimensional (hexahedral) simulation (fig. 19) with wrinkle depths in the range $u_z = 0.002 - 0.0035mm$. The general propagation trend of the wrinkles can be closely predicted by LST simulation. For example, during the displacement increment $u_y = 1.65mm$ to $u_y = 2.00mm$, wrinkles develop rapidly and tend to propagate within most elements. Of course, using a membrane element it is not possible to predict the directions of a continuous or complete wrinkle, but adjacent elements exhibiting wrinkling may infer the existence of a complete wrinkle. For the purposes of identifying the onset and extent of wrinkling the LST formulation is shown to work well.

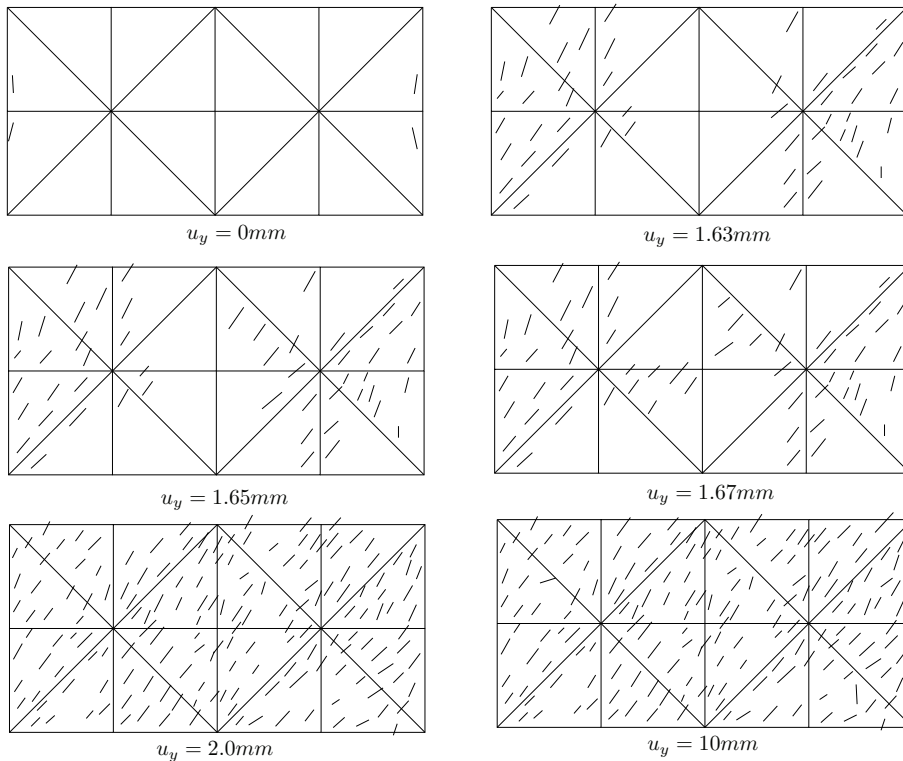


Figure 21: Detected wrinkle points and directions for selected shear displacement u_y - LST

9.2.1 Wrinkling - torsion test

To investigate the wrinkling formula, a torsion test of an annulus membrane given in A. Jarasjarungkiat et al, (2008) is simulated using the 6 node LST element. A flat circle membrane has a outer radius of 12.5m and a hole of 5.0m radius in the center and both of outer and inner boundary are fixed in the rigid rings. The inner rigid ring is rotated counter-clockwise until an angle of 10° is reached. The membrane is discretised by 48 LST element and both isotropic and orthotropic material property are assumed as difference cases as figure 22,

Different from the propagation process in the wrinkling - shear test, as the inner ring is rotated, the wrinkles appears in the whole membrane area under both material assumptions as the inner ring rotate as presented in figure 23. Isotropic membrane has a circle-symmetric wrinkling pattern, and the angles between the wrinkles and ra-

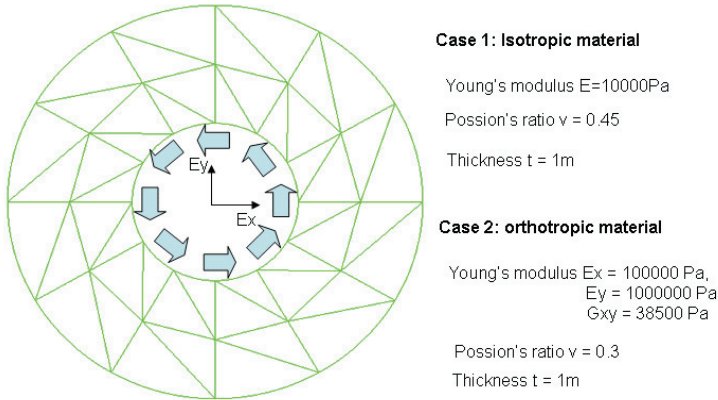


Figure 22: A circle membrane with a hole

radius directions are reduced smoothly along the radius direction from the inner ring to the outer ring. The Orthotropic membrane has different wrinkle patterns that in the top left and bottom right area, the wrinkle directions are approximately parallel or to the radius direction, while in the top right, and bottom left area, the wrinkling directions are roughly parallel to the hoop direction. Compared with the reference result, the a generally good wrinkling pattern under both material assumption may be provided using LST model with the wrinkling procedure.

The stress evaluation is also carried and the maximum principal stresses generated using the LST model is illustrated and compared with the referenceA. Jarasjarunkiat et al, (2008), as figure 24 and 25.

Before the wrinkling procedure applied, the elements work similarly as the thin shell element, and the maximum principal stresses is lower compared with the result from the LST model and the reference. Compared with the reference result, the top value of the maximum principal stresses by LST wrinkling model is close in the isotropic case, but much lower in the orthotropic case. This is because in the wrinkling procedure, the compression stresses are not eliminated while reduced to some level, for example 1/10 of the original values to avoid a hard solution process, which is also presented by the reference for the orthotropic case.

9.2.2 Doncaster Creche canopy

The application of the proposed element formulation to the analysis of an actual membrane structure is demonstrated here by the analysis of the "Creche Canopy",

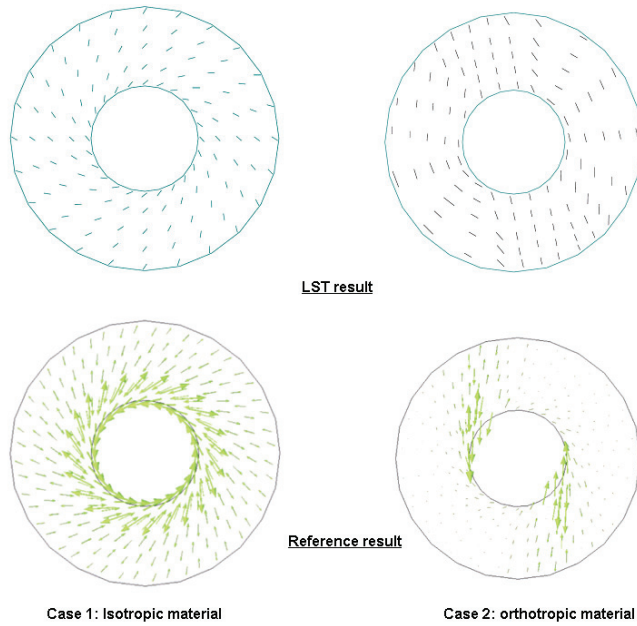


Figure 23: Wrinkling patterns

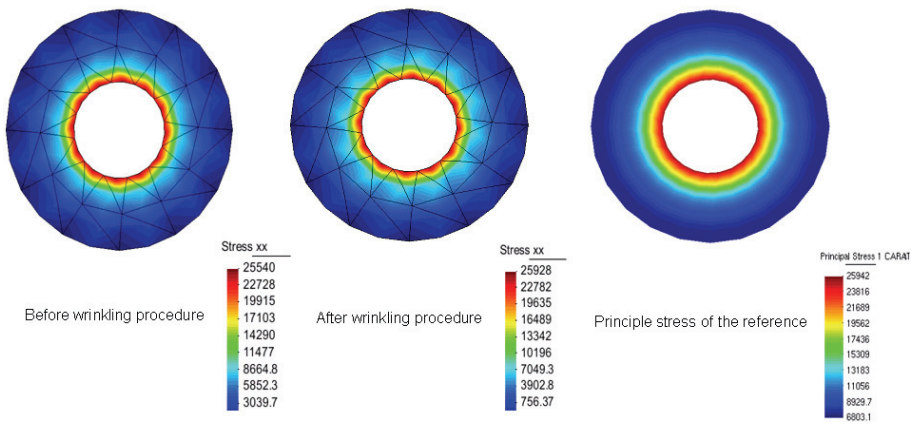


Figure 24: The comparison of the maximum principal stresses under the isotropic material assumption

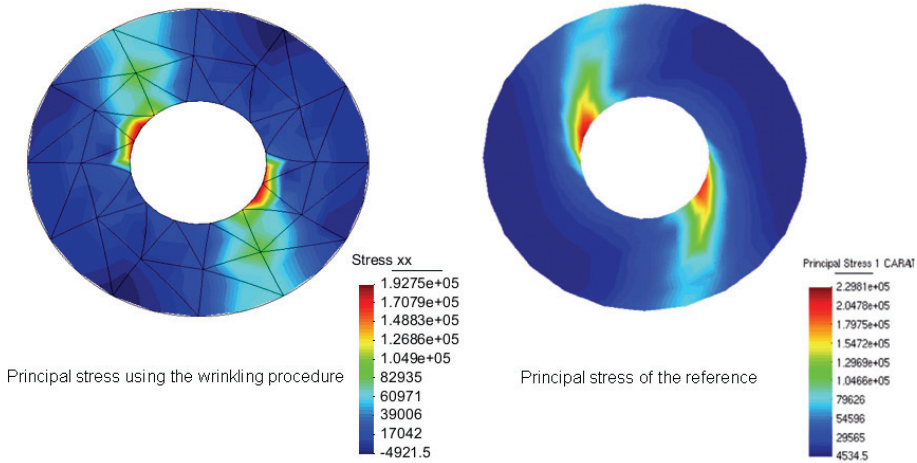


Figure 25: The comparison of the maximum principal stresses under the orthotropic material assumption

Doncaster, UK, designed by Arup and depicted in figure.26.

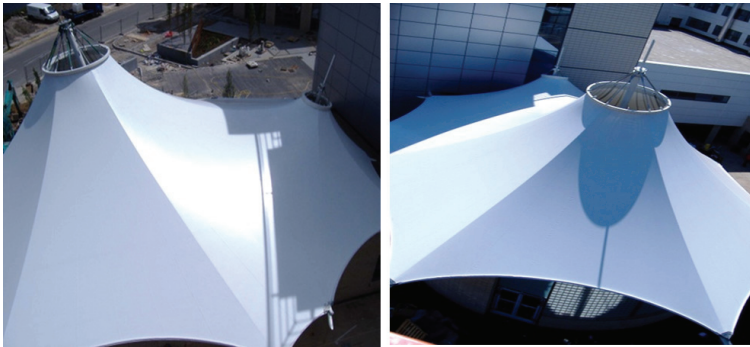


Figure 26: Creche Canopy in Doncaster (Arup)

As shown in fig.27 and 28, the PVC-polyester canopy comprises two conics. Structural support is provided by masts and steel rings at the center of each cone. Radial booms and tensioned cables, plus boundary cables fix the extremes of the fabric, whilst belts are include within the fabric at these locations to control the form.

The prestress of the membrane is 1.5 kN/m along the fill and warp directions. The pretensions of the cables and belts are presented in fig.27. The membrane surface

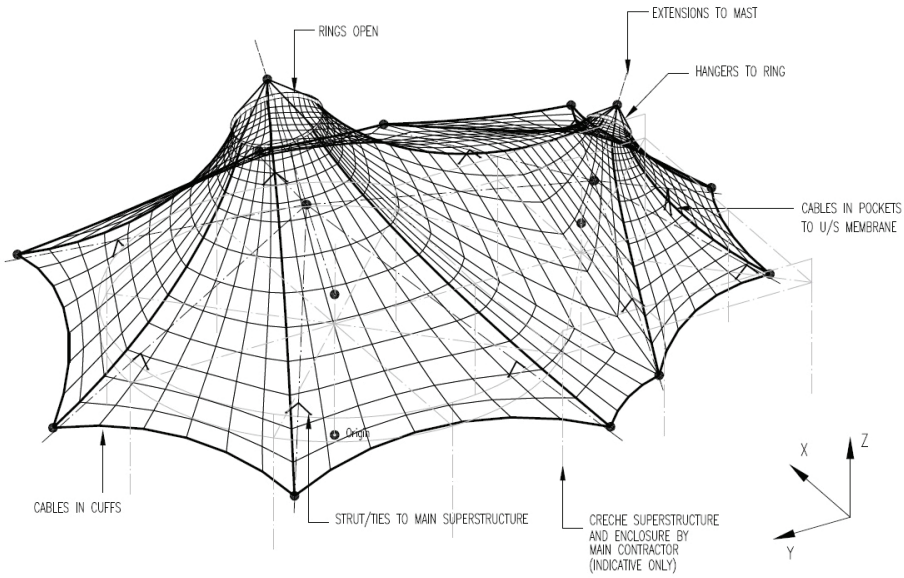


Figure 27: Design plan of Creche Canopy in Doncaster (Arup)

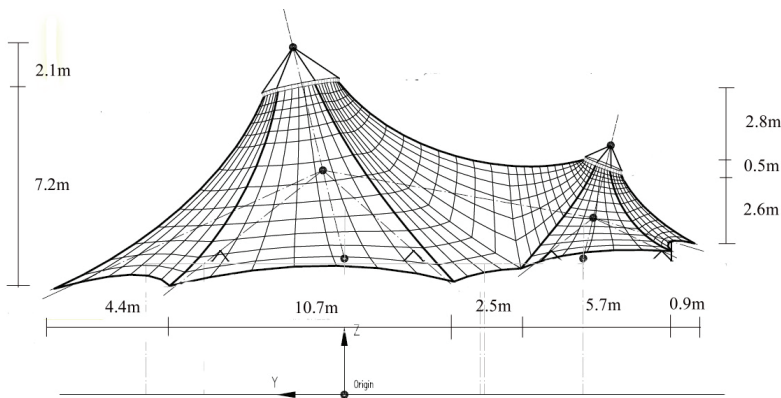


Figure 28: Elevation plan of Creche Canopy in Doncaster (Arup)

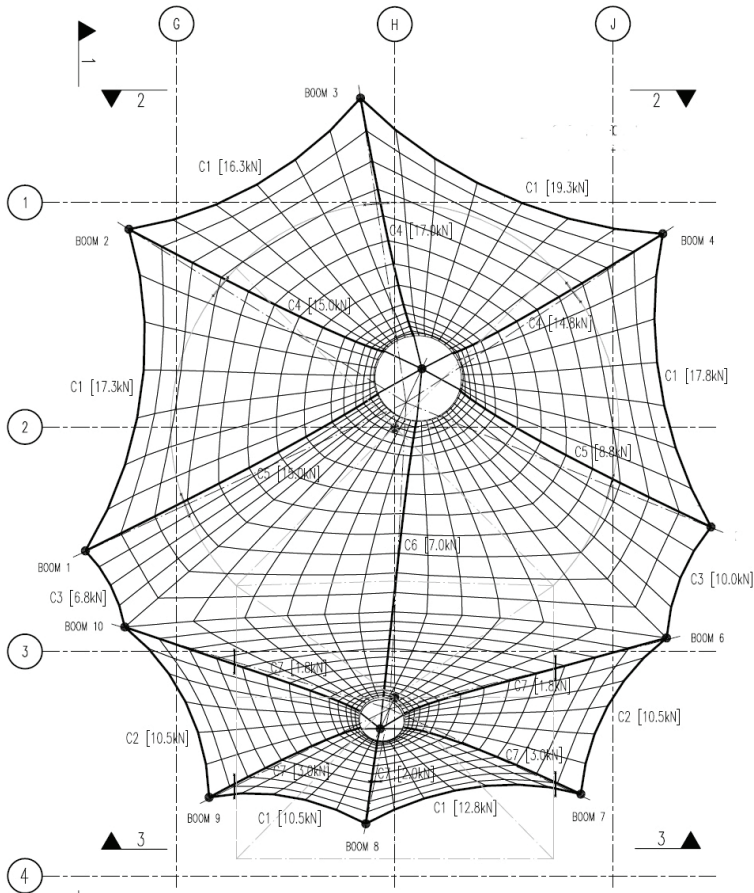


Figure 29: Pretensions in cables and belts of Creche Canopy (Arup)

is discretized by 166 LST elements. The equilibrated prestressed (form-found) geometry is illustrated in fig.30.

The loading analysis assumed the following input parameters: fabric elastic modulus: $E_f = E_w = 1000kN/m$, $G_{yx} = 30kN/m$, Poisson's ratio: $\nu_{wf} = 0.1$, membrane thickness: $t = 0.32mm$; steel cable elastic modulus: $E = 156.8 \times 10^6kN/m^2$; cable cross-sectional area: $A = 216.6mm^2$; uniform (snow) load in vertical direction (Z): $F_z = -0.1kN/m^2$.

The nodal displacements arising from the effect of the uniformly applied load are illustrated in fig.31, with the corresponding membrane stress distributions presented in fig.31 to fig.32. Owing to the strong stiffness of the cables and belts compared

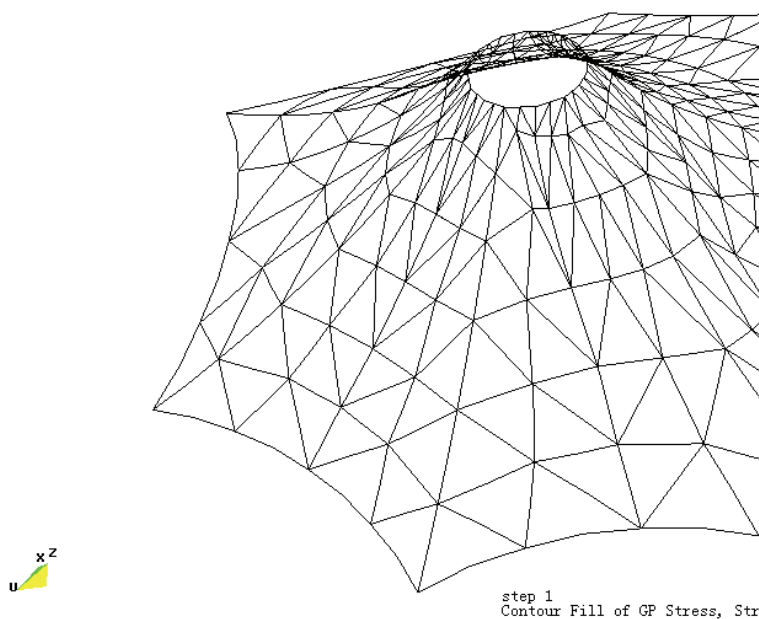


Figure 30: Form-finding of Creche Canopy using 656 LST elements

with fabric, the displacement values of nodes near the belts are very low, while large nodal displacements appear in the membrane remote from the belts. Several displacement "ponds" are formed within the areas defined by the belts. The maximum displacement is located in the area close to the interface between the two component conics as depicted in fig.31.

As shown in fig.32 and 33, the membrane stress distribution is clearly related to the belt positions, and smooth stress distributions are limited to the areas between the belts. In the area around the interface of the two cones, generally the maximum or peak stresses are along the Y direction, while in the two outer perimeter areas, most significant stresses along X direction are observed. Maximum stresses along in directions are observed near the support head rings, where the stress distribution appear less smooth because of the integrated effects from belts and rings in these

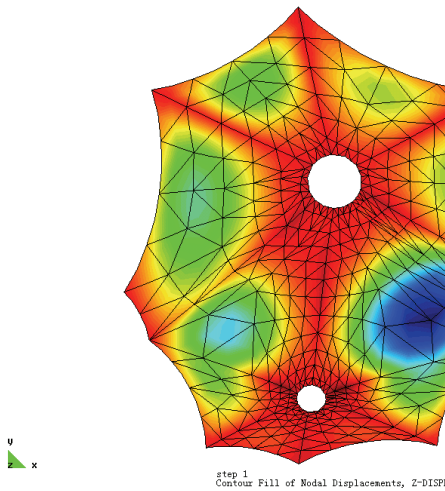


Figure 31: Nodal displacement in vertical direction

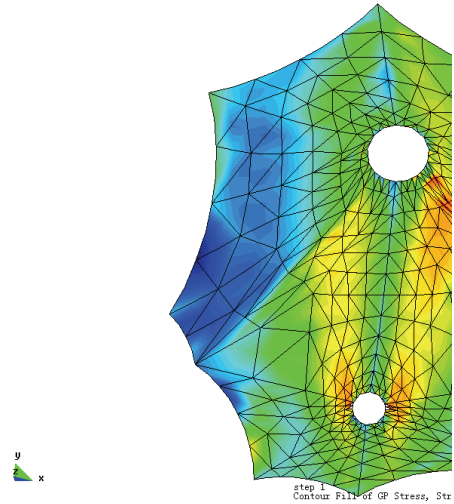


Figure 32: Membrane stress along global y axis

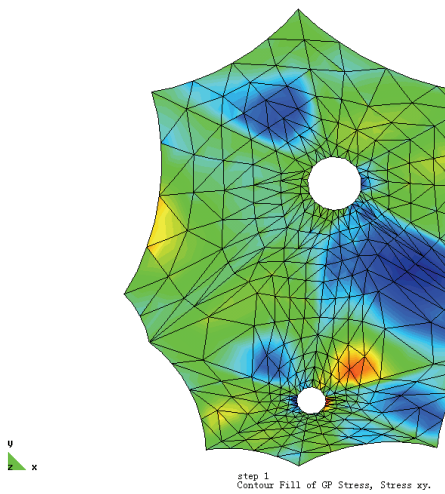


Figure 33: Membrane stress along global x axis

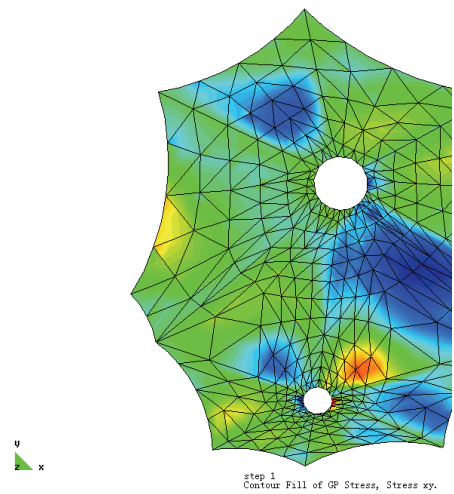


Figure 34: Membrane shear stress across global xy axis

areas.

9.3 Relative compute performance

The absolute and relative performance of the proposed LST formulation coupled with dynamic relaxation (DR) and the Newton-Raphson algorithm is illustrated in figs.35 & 36 as a function numbers of DOF and numbers of elements, respectively. Whilst this is a limited, initial study, it provides some interesting and encouraging data.

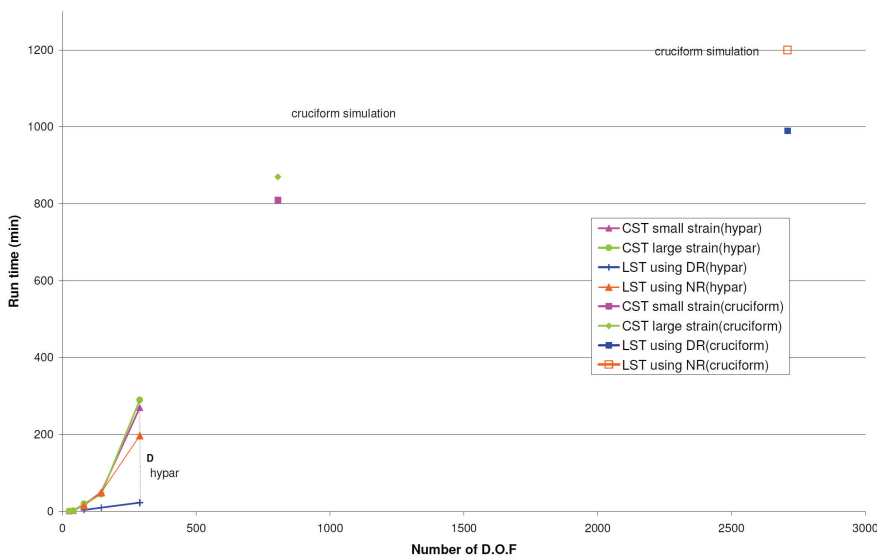


Figure 35: Comparison of computing cost between CST and LST formulations with element number – Hypar and Cruciform test

For example, in the case of the hypar example (§9.1) it is clear that the LST formulation is extremely competitive, providing a high quality solution at little additional computational cost. Normalised or fixed by DOF (e.g fig. 35, area D) the LST requires a small fraction of the computational effort of the CST when coupled with DR, whilst the co-linearity of the plots related to the analysis of the hypar as a function of the number of elements in the discretisation (e.g fig. 36), indicates that a higher quality solution may be achieved using the LST. A similar comparison between the LST coupled with DR or Newton-Raphson solvers clearly shows that DR is the more efficient allgorithm in the analysis of the hypar irrespective of the

basis of the comparison.

From a purely computational cost perspective, the LST performs less well when compared with the CST in the analysis of the cruciform. However, the penalty is small compared with the detail in the solution. It may also be noted that the cruciform exhibits no out-of-plane curvature. Therefore, the advantage of introducing this feature (without additional DOF, nevertheless) is not realised in this particular problem.

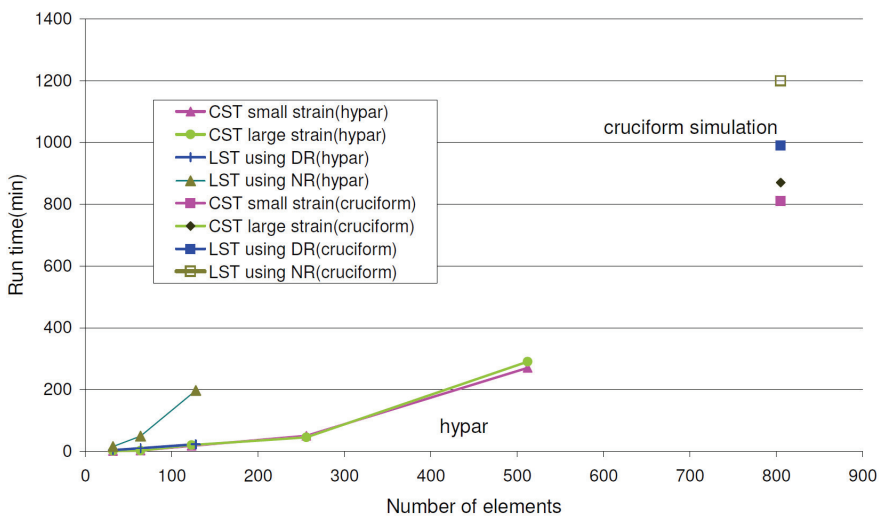


Figure 36: Comparison of computing cost between CST and LST formulations with element number – Hypar and Cruciform test

10 Conclusions

A six node linear strain membrane formulation has been developed using finite element principles. It is based on Green’s strains, but also makes use of inferred element curvatures. No additional rotational D.O.F are included, so the element remains C_0 continuous.

This element formulation passes the patch and is shown to perform well against other tests of element quality. The advantage of having the capability of strains and

stresses that can vary linearly across the element has been clearly demonstrated by a number of solutions compared with the equivalent CST results.

The six-node linear strain triangular element may exhibit particular forms of element distortion that have the potential compromise numerical stability and solution accuracy, with specific reference to the form-finding analysis. A number of element distortion coefficients have been identified in the literature. However, all of these have some or a considerable computational overhead. They are also difficult to interpret in combination. A better measure has been shown to be the criterion that the Jacobian at each of the element Gauss Points remains positive definite. The possibility of "floating" mid-side nodes (e.g. a type of nodal rigid-body motion) has also been examined and deemed to be unlikely to happen in an analysis.

From a normal finite element technology viewpoint associated with Newton-Raphson as the solver, it would be expected that the LST would be considerably more computationally expensive than the CST. However, when coupled with Dynamic Relaxation algorithm, the LST element has been shown to be extremely competitive, producing much higher quality solutions for very little additional computational effort. It has been concluded for the relatively small number of examples examined, that a mesh of LSTs is very well-suited to the the Dynamic Relaxation algorithm and that characteristics of the formulation coupled with this algorithm do not lead to the computational scaling normally seen when moving from a basic to a higher-order element. The capabilities of the element have also been demonstrated on the analysis of an actual membrane structure.

References

Forster B.F., et al (2004): European Design Guide for Tensile Surface Structures, ISBN 908086871x, 2004.

Otto, F (1971): Tensile structures . MIT Press, Cambridge, MA. 1971

Barnes, M. R. (1999): Form finding and analysis of tension structures by Dynamic Relaxation, *Int J of Space Structures*, 14, No 2,89-104, 1999

Gosling, P.D. et al (1996): Optimal structural membranes-I.Formulation of a curved quadrilateral element for surface definition. *Comput.Structs.* Vol 61.No 5.pp 871-883,1996.

Valdes, J.G., et al (2009): Nonlinear finite element analysis of orthotropic and prestressed membrane structures *Finite Elements in Analysis and Design*, v 45, n 6-7, p 395-405, May 2009.

Bridgens, B.N., et al (2004): Tensile fabric structures: Concepts, practice & developments, *Structural Engineer*, v 82, n 14, p 21-27, July 20, 2004.

Ye Xiaobing (1998): Analysis theory of membrane structure by curved surface finite element method. *Journal of Building Structures(Chinese)*, vol 19, n 5, pp 17-21, 1998.

Day, A.S. (1965): An introduction to Dynamic Relaxation, *The Engineer*, 218-221, 1965.

Barnes, M.R. (1980): Non-linear numerical solution methods for static and dynamic analysis of tension structures, Symposium on Air Supported Structures, IStructE, London, 1980.

Kashiwa, M. (2009): Wrinkling analysis using improved dynamic relaxation method, *AIAA Journal*, v 47, n 7, p 1601-1607, July 2009

Schek, H.J. (1973): Force densities method for form finding and computation of general networks, *Int Assoc for Shell and Spat Struct*, p 256-270, 1973

Pauletti, R.M.O. (2008): The natural force density method for the shape finding of taut structures, *Computer Methods in Applied Mechanics and Engineering*, v 197, n 49-50, p 4419-4428, September 15, 2008

Otto, F. (1962): Zugbeanspruchte Konstruktionen, vol. 1 & 2, Ullstein Verlag, 1962.

Miller, R.K., et al (1985): Finite element analysis of partly wrinkled membranes, *Comput.Struct.* 20(1985) 631-639.

Roddeman, D.G. (1987): Force transmission in wrinkled membranes, Ph.D thesis, Eindhoven University of Technology, 1987.

Bletzinger, K.-U. (2008): A wrinkling model based on material modification for isotropic and orthotropic membranes, *Computer Methods in Applied Mechanics and Engineering*, v 197, n 6-8, p 773-788, January 15, 2008

Grundig, L. (1988): Minimal surface for finding forms of structural membranes. *Computer & Structures* Vol. 30, No. 3, pp. 679-683, 1988.

Mitchell, A.R. et al (1971): Forbidden shapes in the finite element method. *J.Inst.Maths Applics*(1971) 8, 260-269.

Baart, M.L. (1986): Quadratic Transformations of Triangular Finite Elements in Two Dimensions. *IMA Journal of Numerical Analysis* (1986) 6, 475-487.

Cook, R.D., et al (1989): Concepts and applications of finite element analysis. Third Edition, University of Wisconsin - Madison (1989), pp 185.

Ishii, K. (1989): Numerical methods in tension structures, Proceedings of the Conference on 10 years of Progress in Shell and Spatial Structures, IASS, Madrid 1989, pp. 3.

Lo, S.H. (1989): Generating quadrilateral elements on plane and over curved surfaces. *Computers and Structures* 1989;31;421-6

Lo S.H. (1985): A new mesh generation scheme for arbitrary planar domains. *International Journal for Numerical Methods in Engineering* 1985;21:1403-26.

Rossi, R. (2003): Convergence of the modified material model for wrinkling simulation of light-weight membrane structures. *Textile composites and inflatables structures* 2003

Liu, X. (2001): Large deflection analysis of pneumatic envelopes using a penalty parameter modified material method. *Finite element analysis and design* 37(2001) pp233-251.

Rossi, R. (2005): Simulation of light-weight membrane structures by wrinkling model. *Int. J. Numer. Meth. Engrg.* 2005; 62:2177-2153

Bridgens, B.N. (2006): Architectural fabric properties: determination, representation & prediction, Chapter 3 ,PhD Thesis in Structural Engineering, University of Newcastle Upon Tyne,UK,2006.

Zhang, L. (2010): Reliability analysis of fabric structures, Newcastle University, UK.

LUSAS Finite Element System, FEA Ltd, Kingston-upon-Thames, UK.

Jarasjarungkiat, A. et al (2008): A wrinkling model based on material modification for isotropic and orthotropic membranes. *Comput. Methods. Appl. Mech. Engrg.* 197(2008) pp773-788.

